Climate sensitivity and meridional overturning circulation in the late Eocene using GFDL CM2.1

David K. Hutchinson[1], Agatha M. de Boer[1], Helen K. Coxall[1], Rodrigo Caballero[2], Johan Nilsson[2] and Michiel Baatsen[3]

5 [1]Department of Geological Sciences, Stockholm University, 10691 Stockholm, Sweden
[2]Department of Meteorology, Stockholm University, 10691 Stockholm, Sweden
[3]IMAU, Utrecht University, Princetonplein 5, 3584CC Utrecht, the Netherlands

Correspondence to: David K. Hutchinson (david.hutchinson@geo.su.se)

10 **Abstract.** The Eocene-Oligocene Transition (EOT), approximately 34 Ma ago, is an interval of great interest in Earth's climate history, due to the inception of the Antarctic ice sheet and major global cooling at the time. Climate simulations of the transition are needed to help us interpret proxy data, test mechanistic hypotheses for the transition, and determine the climate sensitivity at the time. However, model studies of the EOT thus far typically employ control states designed for a different time period,

15 or ocean resolution on the order of 3°. Here we developed a new higher resolution paleoclimate model configuration based on the GFDL CM2.1 climate model adapted to a late Eocene (38 Ma) paleogeography reconstruction. We employ an ocean resolution of 1° x 1.5°, and an atmosphere resolution of 3° x 3.75°. This represents a significant step forward in resolving the ocean geography, gateways and circulation in a coupled climate model of this period. We simulate the model under 3

20 different levels of CO_2; 400, 800 and 1600 ppm. The model exhibits relatively high sensitivity to CO_2 compared with other recent model studies, and thus can capture the expected Eocene high latitude warmth within observed estimates of atmospheric CO_2. However, the model does not capture the low meridional temperature gradient seen in proxies. Equatorial sea surface temperatures are too high in the model (30-37°C) compared with observations (max 32°C), though observations are lacking in the

25 warmest regions of the western Pacific. The model exhibits robust bipolar sinking in the North Pacific and Southern Ocean, which persists under all levels of CO_2. North Atlantic salinities are too fresh to permit sinking (25-30 psu), due to surface transport from the very fresh Arctic (~20 psu), whose

salinities approximately agree with Eocene proxy estimates. North Atlantic salinity increases by 1-2 psu when CO_2 is halved, and similarly freshens when CO_2 is doubled, due to changes in the hydrological cycle.

1 Introduction

5   The Eocene-Oligocene Transition (EOT), approximately 34 Ma ago, was one of the major climate transitions in the Cenozoic Era. The EOT marks the shift from the so-called 'greenhouse world' to the 'icehouse world', during which time the first semi-permanent ice sheets formed on Antarctica, and major changes occurred in flora and fauna across the globe reflecting a shift to colder or drier conditions (Coxall and Pearson, 2007; Dupont-Nivet et al., 2007; Miller et al., 1991). Yet the causes of the

10   transition and its global impacts are still not fully understood, particularly regarding role of the ocean circulation. The leading theories of what caused the transition are: a decline in atmospheric CO_2 below a critical threshold (DeConto and Pollard, 2003), and the opening of Southern Ocean gateways causing thermal isolation of Antarctica (Kennett, 1977); with orbital forcing playing a key role as trigger and pacemaker of ice growth on Antarctica (Coxall et al., 2005).

15

A long-term decline in atmospheric CO_2 has been found to be a major driver of Eocene cooling (Anagnostou et al., 2016), and a plausible trigger of the EOT glaciation (DeConto and Pollard, 2003). This mechanism is appealing in its simplicity, however the threshold required to trigger the glaciation is uncertain. Gasson et al. (2014) found the glaciation threshold to be within a range of 560 to 920 ppm

20   using an intercomparison of late Eocene climate models to force an ice sheet model. This large range was primarily due to the spread in climate sensitivity of the models, of between 2.5°C and 4.1°C per doubling of CO_2 under modern conditions. Observations of CO_2 at the EOT are similarly uncertain, with estimates from carbonate microfossils providing an uncertainty range of 450 to 1500 ppm with a central estimate of 760 ppm (Pearson et al., 2009). Strong CO_2 forcing has had considerable success in

25   explaining the very warm climate of the early Eocene (Huber and Caballero, 2011). The subsequent increase in seasonality and meridional temperature gradient from the early to late Eocene supports the idea that CO_2 forcing had a primary role in Eocene to Oligocene climate change (Eldrett et al., 2009).

Climate
of the Past
Discussions

The evolution of the oceanic meridional overturning circulation (MOC) around the EOT remains a topic of debate. Global compilations of benthic foraminiferal stable isotopes of $\delta^{13}C$ and $\delta^{18}O$ have been interpreted to indicate that the deep ocean was largely homogeneous during the early to middle Eocene

5 (Cramer et al., 2009). This has been used to infer a predominance of southern hemisphere high-latitude deep-water formation. Subsequent divergence of inter-basin benthic isotopic gradients creating oceanic heterogeneity has been linked to onset of North Atlantic intermediate water formation in the late Eocene, and the beginning of a more mature North Atlantic deep water formation in the early Oligocene (Borrelli et al., 2014). In those studies, the proposed forcing mechanism of North Atlantic deep water is

10 the opening of Southern Ocean gateways. This rests on the modern-climate interpretation that mechanical mixing and wind-driven upwelling in the ACC are major drivers of the Atlantic MOC (Toggweiler and Samuels, 1995). Recent modelling suggests that deepening of the Greenland-Scotland Ridge may be a trigger for the onset of North Atlantic sinking (Abelson and Erez, 2017), and the resulting changes in heat transport could also have important effects on the period's climate.

15

In contrast to the North Atlantic sinking hypothesis, Nd isotope distributions suggest that North Pacific sinking occurred all the way from the Cretaceous through to the Miocene (Ferreira et al., 2018). Nd tracer-enabled ocean simulations that are able to reproduce the observed pattern of Eocene Nd data have vigorous bipolar Pacific sinking, with southern rather than North Pacific bottom water dominating

20 (Thomas et al., 2014). Furthermore, idealized GCM simulations show that salt advection feedbacks create a competition between North Pacific and North Atlantic deep water formation (Wolfe and Cessi, 2014), so that the onset of North Atlantic sinking may imply a shutdown of North Pacific sinking and vice versa. It remains unclear if such a switch occurred at the EOT, and its potential triggers have not been fully explored.

25

Modelling studies investigating the effect of the Antarctic Circumpolar Current (ACC) on global climate have found that opening the Drake Passage leads to cooling of the Southern Ocean and a reduction in poleward heat transport towards Antarctica (Cox, 1989; Sijp et al., 2009; Sijp and England,

2004). These studies used either ocean-only or intermediate complexity climate models lacking dynamic atmospheric feedbacks. The Antarctic response of fully-coupled climate models to Drake Passage opening is less clear, since the opening of a circumpolar gateway does not guarantee a strong Antarctic Circumpolar Current under late Eocene paleogeography (Zhang et al., 2010), or under the

5   high CO_2 (Lefebvre et al., 2012) prevalent in the late Eocene. Furthermore, there is uncertainty of up to tens of millions of years over when a deep gateway first existed in Drake Passage (Barker et al., 2007; Livermore et al., 2005), so that the inception of the ACC cannot be easily pinpointed to the EOT. The opening of a deep Tasman Seaway has also been suggested to occur around the EOT and cause Antarctic glaciation (Stickley et al., 2004). A model study of this opening found that the gateway

10 change had a limited effect on Antarctic surface climate (Sijp et al., 2011). However, the gateway change may explain ~3°C of deep ocean cooling (Sijp et al., 2014), in agreement with late Eocene cooling found in deep sea foraminifera (Bohaty et al., 2012). Part of the CO_2 decline at the EOT may have been caused by the opening of Southern Ocean gateways (Elsworth et al., 2017), due to feedbacks in silicate weathering. This presents a possible way to reconcile the CO_2 forcing and gateway

15 hypotheses.

A common shortcoming of previous EOT simulations is an unrealistic representation of topography (by 'topography' we mean both land topography and ocean bathymetry). Many studies investigating gateway effects have used modern topography for their control simulation (Elsworth et al., 2017;

20 England et al., 2017; Fyke et al., 2015; Sijp et al., 2009; Yang et al., 2014) and created EOT-like perturbations by closing Drake Passage and/or opening the Panama Seaway. While this method of changing basin geometry is appealing in that it illuminates specific gateway effects, it implicitly ignores several features of the late Eocene or early Oligocene paleogeography that are potentially crucial to the ocean circulation. These include particularly the closed Pacific-Arctic Bering Sea seaway, the narrower

25 Atlantic Basin, the shallow connections between the Atlantic and the Arctic, and the connections of the Tethys Ocean with the Indian and Arctic Oceans (Figure 1). Other modelling studies of the EOT have been configured with early Eocene (~55 Ma) paleogeography. These have particularly focused on the effects of changing CO_2 forcing from the Eocene to the Oligocene (Eldrett et al., 2009; Liu et al., 2009),

the impact of an ice sheet on the atmosphere and ocean circulation (Goldner et al., 2013, 2014), and the impact of opening Southern Ocean gateways (Goldner et al., 2014). While early Eocene topography is a much closer starting point to late Eocene topography than modern, it does not capture the subsequent ~20 Ma of tectonic evolution. This includes the gradual opening of the Tasman Gateway and Drake

5 Passage, and the widening of the Atlantic.

Some recent climate model studies have used reconstructions of late Eocene and early Oligocene topography for their control runs (Kennedy et al., 2015; Ladant et al., 2014; Lefebvre et al., 2012; Lunt et al., 2016; Zhang et al., 2010). Kennedy et al. (2015) found that when an ice sheet is placed over

10 Antarctica, the Pacific sector of the Southern Ocean surface warms significantly when the Tasman Seaway is constricted as in the late Eocene, whereas when the Tasman Seaway is wider as in the early Oligocene, there is instead a weak cooling. These results contrast with Goldner et al. (2014), who found a strong cooling of the Southern Ocean in response to Antarctic glaciation, albeit with an early Eocene paleogeography. Thus, there remains uncertainty over whether the opening of Southern Ocean gateways

15 caused major cooling, or whether the glaciation itself was the primary driver of Southern Ocean temperature change.

Model studies of the EOT, including those mentioned above, generally employ very low - typically 3° - horizontal ocean resolution. This is often a necessity of computational constraints, since the deep ocean

20 takes thousands of years to equilibrate (Danabasoglu et al., 1996). Furthermore, uncertainties in the reconstructed paleogeography often place limitations on the fidelity of the relevant topographic features. We are interested in improving the ocean resolution for two reasons. First, the Arakawa B-grid used ubiquitously in paleoclimate model studies requires narrow ocean straits to be at least 2 grid cells wide, in order to have a non-zero velocity grid point. If a model uses 3° resolution, then the minimum width

25 of a strait is 6°, corresponding to 670 km in the meridional direction. In the zonal direction, 6° of distance varies from 670 km at the equator to 330 km at 60° latitude. These distances are large enough that key EOT ocean gateways, such as Drake Passage and Arctic gateways will hardly be resolved. Second, there is evidence that gateway effects are enhanced at higher resolution (Viebahn et al., 2016),

especially in controlling the heat transport of boundary currents. For example, moving from 1° to 0.25° (eddy-permitting) resolution in the modern-day climate results in an enhanced western boundary current heat transport (Delworth et al., 2012), and this effect can cause substantially lower Arctic sea ice coverage (Hutchinson et al., 2015; Kirtman et al., 2012). Moving from 3° to 1° ocean resolution, while

5   still not permitting eddies, would improve the representation of boundary currents and their associated impacts on gateway transitions.

This study presents a new fully-coupled climate simulation of the late Eocene using order 1° ocean resolution and a state-of-the-art paleotopographic reconstruction. We apply the late Eocene (38 Ma)

10 reconstruction of Baatsen et al. (2016) to generate topography for the GFDL CM2.1 model, as shown in Figure 1. This ensures that global tectonic evolution relevant to the late Eocene is included, and any future perturbations to ocean gateways or other boundary conditions are referenced to a control state that is specifically designed for the late Eocene. Within this framework, we explore the climate sensitivity to CO_2 perturbations, namely using 400, 800 and 1600 ppm (approximately 1.4x, 2.9x and

15 5.7x preindustrial CO_2 respectively). We also explore the sensitivity to changing the vertical diffusivity from the standard Bryan-Lewis scheme to a tidal-mixing scheme where mixing is set to a constant background value and then enhanced in the vicinity of rough topography. We examine the impact of these changes on the oceanic MOC and global climate.

2 Model Description

20 ### 2.1 Model Components

This study uses a modified version of the coupled climate model GFDL CM2.1 (Delworth et al., 2006), using boundary conditions for the late Eocene. The ocean component is updated to the modular ocean model (MOM) version 5.1.0, while the other components of the model are the same as in CM2.1, namely Atmosphere Model 2, Land Model 2 and the Sea Ice Simulator. In the ocean and sea ice

25 components, the horizontal grid is modified to have a resolution of 1° latitude x 1.5° longitude. We use a tripolar grid as shown in Figure 7 of Murray (1996), with a regular latitude-longitude mesh south of

65°N, and a transition to a bipolar Arctic grid north of 65°N. The poles then lie over North America and Siberia to avoid convergence of meridians in the Arctic Ocean. This enables the model to simulate Arctic Ocean velocities without damping in the vicinity of the North Pole. Unlike in CM2.1, there is no refinement of the latitudinal grid spacing in the tropics. The ocean retains the original 50 vertical levels

5   with the same grid spacing as in CM2.1. The atmospheric horizontal grid resolution is 3° x 3.75°, with 24 vertical levels. This atmosphere grid is identical to that used in CM2Mc (Galbraith et al., 2010). This choice of grid resolutions gives good load balancing between the atmosphere and ocean components, while enabling better resolution of coastlines and straits than most existing Eocene models (~3° ocean resolution).

10

The topography is adapted to our model grid using the late Eocene (38 Ma) reconstruction of Baatsen et al., (2016). Manual adjustments were made to the topography to ensure that all straits are at least 2 grid cells wide, so that they have corresponding velocity grid points, and no ocean grid cell is isolated. The resulting ocean bathymetry is shown in Figure 1a. In the atmosphere, the topography is interpolated

15   onto the horizontal grid and then smoothed using a 3-point mean filter to ensure a smoother interaction with the wind field. The resulting topography is shown in Figure 1b. Vegetation types are based on a dataset based on Sewall et al. (2000), with modifications where data are available from Thorn and DeConto (2006); Utescher and Mosbrugger (2007); and Gomes Rodrigues et al. (2012). The Sewall et al. (2000) dataset was originally configured for the CESM plant functional types, and we have adapted

20   these to the corresponding vegetation type in CM2.1. The river runoff is determined by a relocation map, where each land point is assigned a corresponding coastal location for returning runoff to the ocean. This relocation map was determined by a downslope relocation algorithm from the model topography. Aerosol forcing was taken from the Eocene (55 Ma) reconstruction of Herold et al. (2014), and adapted to our model's input types.

25   **2.2 Vertical Mixing Scheme**

We use a simplified version of the tidal mixing scheme of Simmons et al. (2004). The CM2.1 code distribution provides a heterogeneous distribution of seafloor roughness amplitude based on high

resolution maps of the modern seafloor. We set this to be uniform for simplicity, since estimating the late Eocene seafloor roughness is not straightforward. We thus calculate an average roughness amplitude of 210.512 m (the h parameter from Eq. (1) of Simmons et al. 2004), and set a background diffusivity of 1.0×10^{-5} m^2 s^{-1}. In parallel we also simulate the model using the standard Bryan-Lewis

5   diffusivity in CM2.1, commonly used in deep time paleoclimate studies (e.g. Lunt et al. 2012). We prefer a bottom roughness mixing scheme to Bryan-Lewis, since the Bryan-Lewis scheme is specifically tuned to modern observations of mixing which are in turn dependent on bathymetry. These mixing rates may be different in deep time paleoclimates. Using the tidal-mixing scheme, the structure of the thermocline is thus able to adjust to the altered geography and different climate conditions of the

10   Eocene.

2.3 Initial Conditions and Spinup

The initial conditions of the ocean model are configured to a modified version of the DeepMIP experimental design (Lunt et al., 2017). The temperature and salinity are set to the following profiles:

15   T [°C] = (5000 − z) / 5000 * 20 cos (ϕ) + 10 ;   if z ≤ 5000 m.

       = 10 ;   if z > 5000 m.

S [psu] = 35.0

where ϕ is latitude, z is depth of the ocean (metres below surface – positive downwards).

20   The model is run at three different levels of CO_2: 400, 800 and 1600 ppm, where 800 ppm is deemed as the control simulation. The atmosphere and land surface components are initialised from a previous test simulation.

We used the following procedure to spin up the model simulations:

25   1.   The model is run in coupled mode for 50 years.
         2.   The last 10 years of this coupled simulation are used to generate surface boundary conditions for an ocean and sea ice only simulation.

3. The model is run in ocean and sea ice only model for 500 years, using a 10-year repeating pattern of forcing based on the CORE protocol (Griffies et al., 2009). During this simulation, we doubled the ocean tracer time step with respect to the momentum time step.

4. The resulting ocean state is used to re-initialise step 1.

5. After 6 cycles of the above (i.e. a total of 3300 model years), the simulation was continued in fully-coupled mode (with no acceleration of tracers) for a further 3200 years.

In order to assess the robustness of this acceleration method, we also ran the control simulation from the same initial conditions for 1000 years in coupled mode only. This coupled-only simulation yielded an ocean state that was very similar in key metrics (i.e. temperature, salinity, age tracer) to the iteratively coupled ocean run at year 2000. In other words, the iterative coupling procedure achieved a climate state that was similar to that of an ordinary coupled run, with roughly twice the number of model years needed to reach the same state. This approximately cancels out the computational speed-up achieved by the decoupling procedure. We therefore abandoned the iterative coupling procedure after 6 cycles and completed the spinup in coupled mode.

The spinup evolution of ocean temperature across the three levels of CO_2 is shown in Figure 2. The simulations all have surface climates in quasi-equilibrium, though the deep ocean is gradually cooling in all cases. All simulations have a temperature trend of less than 0.1°C per century at 4000 m, though the warmer climates are trending more slowly than the colder ones. This is because the initial conditions are designed to be warmer rather than colder than equilibrium, so that convection can readily occur due to surface cooling. The step changes in SST over the first 3300 years are due to the coupling/decoupling procedure described above. We also examined the evolution of the meridional overturning circulation during spinup, and found that both the preferred sinking regions and the magnitude of overturning were steady over the last ~2000 years.

3 Climate and Ocean Circulation

The late Eocene paleogeography incorporates changes that affect important features of the ocean circulation compared with the present day. The Southern Ocean gateways of Drake Passage and the Tasman Seaway are narrow and shallow (sill depths of around 500 m), and permit a weak eastward

5   circumpolar flow. Panama Seaway is open, and allows a shallow connection of surface water between the equatorial Atlantic and Pacific Oceans. The Bering Strait is closed, so that the North Pacific has no direct connection with the Arctic Ocean. The Arctic Ocean is connected to the North Atlantic by narrow and shallow seaways (up to 200 m depth), which allow export of freshwater from the Arctic into the Atlantic. Transport between the Arctic and Atlantic is bidirectional, with surface waters travelling

10   predominantly southwards, and waters below 100 m travelling predominantly northwards. The Tethys Ocean has connections to the Indian and the Atlantic, and a very narrow and shallow connection via Turgai Strait to the Arctic (25 m depth), allowing unidirectional southward transport of surface waters. Apart from these gateway changes, the Pacific is wider and more open through the Indonesian Archipelago, while Australia is further South. The Atlantic is similarly narrower especially in the

15   Northern Hemisphere, and in this region the subpolar gyre is particularly constricted. These features all contribute to a vastly different ocean circulation than present day, and we explore the major changes below.

3.1 Surface Climate

In this section, we describe the control climate (800 ppm), key features of the circulation and how they

20   compare with proxy evidence. Figure 3a and Figure 3b show the sea surface temperature (SST) and surface air temperature (SAT) respectively. Equatorial SSTs reach as high as 38°C in the western Pacific warm pool, with tropical temperatures around 30-35°C elsewhere. The warm pool extends west into the Indian Ocean due to an open Indonesian Seaway. The meridional temperature gradient is a little lower than in the modern climate, with the high latitude SSTs of the North Pacific and Southern Ocean

25   being around 15-20°C, even along the coast of Antarctica.

10

The sea surface salinity (Figure 3c) indicates very fresh conditions in the Arctic Ocean, around 20 psu. The fresh Arctic surface waters flow out primarily into the North Atlantic, where the surface salinities around Greenland and above ~45°N are generally below 30 psu. Under these conditions deep sinking cannot occur in the North Atlantic. On the other hand, the high latitude North Pacific surface water is

5 mostly around 35 psu, apart from a limited region in the north-east where there is strong runoff entering the ocean from the North American mountain ranges. Under modern conditions the orography, via its influences on atmospheric circulation and drainage pathways, forces the surface water in the North Pacific to be fresher than in the North Atlantic (Maffre et al., 2017; Sinha et al., 2012; Wills and Schneider, 2015). Notably, the low surface salinities prevent deep water formation in the present-day

10 North Pacific (Warren, 1983). However, our control simulation shows a higher river runoff (0.28 Sv) going into the Arctic than the North Atlantic (0.14 Sv) and North Pacific (0.15 Sv) (here the cutoff latitude is chosen to be 45°N). The same comparison with a simulation of CM2.1 in its modern configuration produces a river runoff of 0.10 Sv into the Arctic, only slightly higher than North Atlantic of 0.07 Sv and North Pacific of 0.08 Sv. This high Arctic runoff, combined with enhanced P-E forcing

15 of the warm climate creates the very fresh Arctic surface waters. Transport of this fresh Arctic water mass into the North Atlantic causes a state reminiscent of the present day North Pacific with low surface salinity, a strong halocline and no deep water formation.

Zonal wind stress (Figure 3e) in the Southern Ocean has a more zonal structure than in the present day,

20 with a weaker standing wave meander and a lower magnitude overall. The wind stress peak sits around 50°S, similar to present day, and the wind stress curl drives subtropical gyre circulations in the South Pacific and Indian Oceans analogous to the present day, as shown in the barotropic streamfunction of Figure 3f. The Southern Ocean gateways — Drake Passage and the Tasman Seaway — are open, but they are narrow and shallow and thus allow only a weak circumpolar flow around Antarctica of 15 Sv.

25

The mean state of the model has an east-west temperature contrast across the equatorial Pacific in excess of 6°C, slightly stronger than in the present day, suggesting a more La Niña-like mean state. Empirical orthogonal function (EOF) analysis of global SST indicates strongest variability in the central

equatorial Pacific (Figure 4a), while precipitation varies most strongly in a dipole spanning the western equatorial Pacific and Indian oceans (Figure 4b). Using the first EOF of SST, we define an 'El Niño Index' region between 170°E and 140°W, and 5°S to 5°N, as being representative of highest Pacific equatorial SST variability. This index is analogous to the present-day Niño-3.4 index, designed to

5   bracket the region of highest El Niño-Southern Oscillation (ENSO) variability. This index indicates the occurrence of multi-year El Niño and La Niña events (Figure 4c), defined by a threshold of +0.5°C for an El Niño and -0.5°C for a La Niña, as used in present day. The magnitude of temperature deviations is generally weaker than present day Niño-3.4 variability. The east-west SST gradient in the equatorial Pacific is closely anti-correlated with the El Niño index, with a reduction in east-west gradient during El

10   Niño and vice versa for La Niña (Figure 4d). However, the magnitude of these variations is also weaker than present day, suggesting that our model has a more robust western Pacific warm pool than present day. We suggest this reduction in El Niño variability is due to the widening of the Pacific basin and the relative absence of continental barriers such as New Guinea and Indonesia, which are further separated in the late Eocene and create a more permanent and stronger warm pool. This result agrees broadly with

15   von der Heydt and Dijkstra (2006), who also found a stronger western Pacific warm pool in an Oligocene model simulation.

The 'Weddell Sea' equivalent in the EOT model, where deep water forms in the model, has annual mean sea surface temperature below 10°C and develops a small area of seasonal sea ice close to the

20   coast. The Arctic Ocean temperatures are typically around 4-6°C, and it is mostly ice free all year round, apart from some embayments around the Siberian coast. The average maximum monthly sea ice thickness for each hemisphere is plotted in Figure 5, showing September thickness for the Northern Hemisphere and March thickness for the Southern Hemisphere. We note that there is evidence of ice-rafted debris in the Arctic from the middle Eocene onwards (Stickley et al., 2009), indicating the likely

25   presence of seasonal sea ice at this time. Our 400 ppm simulation has Arctic-wide sea ice in summer (Figure 5b), suggesting that the model's sea ice is more accurate at a lower level of CO_2.

3.2 Meridional Overturning Circulation

The meridional overturning circulation (Figure 6) shows a structure of sinking in the North Pacific and Southern Ocean. There is no deep overturning cell in the North Atlantic, due to the surface waters being far too fresh to allow for local deep water formation. The structure of the Pacific overturning is

5   analogous to modern day North Atlantic Deep Water formation: the Northern Component Water is warmer and saltier than the Southern Component water and is heavier at the surface. This difference in deep water properties is caused by colder winter temperatures in the Southern Ocean sinking regions than the North Pacific, since deep water forms exclusively in winter. The colder winter temperatures are due to the asymmetry of landmasses between the poles. One factor is that the Southern Ocean extends

10   further poleward than the North Pacific (in both Pacific and Atlantic sectors). Furthermore, the Antarctic continental interior becomes colder in winter than the Arctic Ocean, and therefore the seasonal cycle in high latitude (>60°) surface air temperature is stronger in the Southern Hemisphere. The Northern Hemisphere also has very cold winters in continental interiors, but its polar winters are moderated by the presence of an ocean and its seasonal cycle is milder.

15

As in modern climate, thermobaric effects control the layering of the abyssal ocean (Nycander et al., 2015). The Southern Hemisphere sourced deep waters are colder and therefore more compressible than the warmer and slightly more saline ones sourced from the Northern Hemisphere. Thus bottom waters are predominantly formed in the Southern Ocean. Sinking occurs in both the Pacific and Atlantic

20   sectors of the Southern Ocean, as indicated by the age tracer at 2000 m and winter mixed layer depths (Figure 7). Both of these sectors contribute to bottom water formation, as can be seen from the age tracer distribution. The shallow gateways through Drake Passage and Tasman Seaway provide barriers that prevent Pacific- and Atlantic-sourced bottom waters from directly penetrating into the opposite ocean basin. The poleward heat transport is similar to modern (not shown), with the partition between

25   ocean and atmosphere heat transport being dominated by the ocean in the tropics only, and by the atmosphere in the mid- to high- latitudes. As in the modern ocean, poleward heat transport is skewed towards the Northern Hemisphere, with a peak value of 2.2 PW (northward) and a minimum value of -0.9 PW in the Southern Hemisphere. We suggest that this asymmetry is due to the analogous

Climate
of the Past

Discussions

asymmetry of deep water formation; i.e. a warmer and saltier northern cell tends to enhance northward ocean heat transport relative to the colder and fresher southern overturning cell. In the tropics, we do not find deep water formation due to warm, salty water masses such as in the Tethys.

5   We also compare the results of our control run with the widely-used Bryan-Lewis mixing scheme, as used in the default case of CM2.1 (Delworth et al., 2006). The shape of the Bryan-Lewis mixing scheme is designed to reflect the modern distribution of mixing rates, in turn shaped by modern geography. Major changes to the bathymetry were expected to alter the deep ocean mixing distribution due to intensified mixing over ridges and rough topography, while large changes to surface radiative forcing

10 may were expected to alter the thermocline structure. However, we find that the meridional overturning circulation and stratification are largely insensitive to this change in vertical mixing. The magnitude of the overturning, distribution of sinking regions and age tracer were all very similar between the mixing schemes (not shown). This was a surprising result, given theoretical predictions of change due to roughness mixing (de Boer and Hogg, 2014). We do find that the abyssal ocean is slightly cooler in the

15 bottom roughness mixing scheme (0.5°C), suggesting a larger separation between the upper cell and the lower cell, in line with theoretical predictions. We also find abyssal salinity differences on the order of 0.1 psu. Given the very long spinup time of the simulations, the lack of divergence between the schemes is surprising. In the Arctic Ocean, the differences in deep ocean temperature and salinity are greater. This is because the deep waters in the Arctic are very stably stratified by the halocline and can only

20 communicate with the surface diffusively.

3.3 Comparison with Proxy Data

A comparison of proxy data with the model SSTs for the 400, 800 and 1600 ppm experiments is shown in Figure 8. The proxy data are taken from the late Eocene compilation of Liu et al. (2009), and include $U^{k'}_{37}$ data, TEX_{86} and Mg/Ca from a time window of 34-37 Ma for the pre-EOT. Two additional data

25 points are added: (i) TEX_{86} data from ODP site 1172 (Bijl et al. 2009), from a time window of 36.5 to 38.5 Ma; and (ii) TEX_{86} data the Tanzania Drilling Program (Pearson et al., 2007), averaged across two late Eocene time points of 33.8 Ma and 39.6 Ma. The paleolocations of these proxies were determined

using GPlates, reconstructed to an age of 38 Ma using the Paleomagnetic reference frame of Torsvik et al. (2012) and van Hinsbergen et al. (2015). This ensures consistency with the model boundary conditions (Baatsen et al., 2016).

5   Figure 8 shows the proxy data points compared with the nearest model ocean point, and the model zonal mean temperature. The 1600 and 800 ppm cases are too warm compared with the proxies in the tropics. In the control case (800 ppm) the model is roughly 3°C warmer at the equator. However, the TEX_{86} data from Tanzania (~32°C) of Pearson et al. (2007) agree better with the control case. In the mid to high latitudes, the control case is colder than the proxy estimates. The 1600 ppm case agrees better with the
10 mid to high latitude proxy estimates, however its warm bias at the equator is very large. In the 400 ppm simulation, the tropical temperatures agree well with the proxies, while in the mid-latitudes, it is too cold.

      The model's inability to capture the low meridional temperature gradient in the proxies is a common
15 problem in simulating warm climates of the Eocene (Huber and Caballero, 2011). However, several apsects of the proxy data could help to improve this situation. First, alternative calibrations of the TEX_{86} data from Tanzania may yield temperatures as high as 35°C in the late Eocene (Bijl et al., 2009), which would reduce the low gradient problem. We also note that there are no available late Eocene proxy estimates in the western Pacific warm pool, where the ocean's warmest temperatures are found. Second,
20 high latitude TEX_{86} data may be affected by summer bias due to seasonal growth of its underlying species (Kim et al., 2010), which may have the effect of reducing the meridional temperature gradient seen in the proxies.

4 Climate Sensitivity to CO2

4.1 Temperature Response

25 The global mean SST in the control run (800 ppm) is 27.8°C; halving CO_2 to 400 ppm produces 3.5°C of cooling, and doubling CO_2 to 1600 ppm yields 4.2°C of warming. The global mean SAT in the

Climate
of the Past

Open Access

Discussions

EGU

control is 25.6°C; halving CO_2 to 400 ppm produces 4.0°C of cooling, and doubling produces 4.8°C of warming. The higher sensitivity of temperature change in the atmosphere is due to both stronger polar amplification in the atmosphere than the ocean; and a stronger temperature change over land than over the ocean. In its modern configuration, CM2.1 has an equilibrium sensitivity of 3.4°C (Winton et al.,

5   2010). The lower sensitivity in the modern case may be due to many factors, for example higher albedo due to the presence of ice sheets, and the higher percentage of land versus ocean. Furthermore, our simulations indicate some state dependence, with higher sensitivity at higher CO_2.

The response of SST and SAT to CO_2 changes is shown in Figure 9. In the 1600 ppm case (Figure 9a,c),

10   the tropics warm by between 3-4°C, with a strong amplification in both of the polar regions. SAT over the Arctic Ocean and over Antarctica are 7-9°C warmer, with the magnitude of polar amplification being similar in both hemispheres. This approximate doubling of warming in the polar regions aligns with expectations from idealised climate modelling of the polar amplification response (Alexeev et al., 2005). The polar amplification is a combination of the local radiative forcing and the enhanced moist

15   energy transport from the tropics. The Arctic Ocean warming is especially pronounced in the 1600 ppm case, despite the absence of ice-albedo feedbacks. We suggest that the ice-free conditions allow for substantial radiative warming of SST in addition to atmospheric polar amplification. Warming over land shows a mixed response; warming over North America and Siberia is enhanced compared with oceanic regions at the same latitude, as is the case in southern Africa. By contrast, other regions such as

20   Australia, equatorial Africa and parts of South America show little change to the land-ocean contrast. This is linked directly with the land-ocean monsoon response in low to mid-latitudes. Regions of enhanced land warming are closely associated with enhanced drying, while regions of reduced land warming generally also become wetter, as shown in the P-E forcing (Figure 10). In the higher latitudes, the monsoonal forcing is weaker, and thus the P-E changes are not as closely linked with the

25   temperature response.

In the 400 ppm case (Figure 9b,d), the magnitude of tropical cooling and polar amplification are similarly strong as in the warming case. The Antarctic SAT response is however somewhat stronger

than the warming case due to the triggering of snow albedo feedbacks. Under 400 ppm, a far greater proportion of the Antarctic continent is covered in snow in winter. The model does not sustain freezing temperatures over Antarctica in summer. However, this should not be interpreted directly as evidence that an ice sheet cannot be triggered under this climate; the model lacks the necessary feedbacks to

5   simulate the accumulation of long term snow and ice (e.g. Gasson et al. 2014). One area of strong cooling occurs in the Weddell Sea, where SSTs drop by ~8°C, with a commensurate change in SAT. There is also a cessation of deep water formation in this region, and the formation of seasonal sea ice in the 400 ppm case (see Figure 5). The Pacific sector of the Southern Ocean cools to a similar magnitude as the warming case. The SST cooling in the Arctic is less pronounced than in the warming case, simply

10   because the sea surface freezes for much of the year and therefore the surface change is limited to ~4°C. The SAT response in the Arctic is similarly strong, showing that the atmosphere polar amplification can be much stronger than the Arctic SST change.

4.2 Salinity and Hydrological Cycle

In response to a doubling of CO_2 to 1600 ppm, surface salinity decreases markedly over the mid and

15   high northern latitudes as shown in Figure 10a. Arctic Ocean salinities decrease by around 1 psu, due to the enhancement of the high latitude precipitation and river runoff into the Arctic. The river runoff accumulates from North America, Europe and Siberia, so the net effect of the increased P-E (Figure 10c) on the salinity is particularly concentrated in the Arctic. This Arctic freshening also has a marked impact on North Atlantic salinity. Conversely when CO_2 is halved, Arctic salinities are enhanced by 1-2

20   psu, due to the weakening of precipitation and runoff into the Arctic.

Salinity changes in other regions also reflect changes in the P-E balance to a lesser extent. The north-east Pacific freshens in response to warming and becomes saltier in response to cooling, due to the same forcing mechanisms. The interiors of the gyre circulations in the Pacific show signatures of the P-E

25   forcing, but the salinity differences are not as clearly correlated here, due to advection and lateral mixing altering the signal. One area of notable increase in salinity under the warming scenario is the southern tropical Pacific, where salinity is greatly enhanced. This corresponds to an area of net drying

Climate
of the Past

Discussions

in the P-E fields, but other regions do not show nearly the same salinity response to the same magnitude of forcing. Clearly advection feedbacks are at play, as evidenced also by the net freshening of the South Atlantic in the 1600 ppm case. This occurs despite a net decrease in P-E over the subtropical South Atlantic gyre. One possible explanation is the enhanced African monsoon, which leads to large river

5   runoff increases from West Africa into the Atlantic. Furthermore, sinking in the Atlantic sector of the Southern Ocean decreases markedly in the 1600 ppm case, which is evident in both the mixed layer depths and age tracers at intermediate depth (not shown). This reduction in deep water formation in turn reduces the salt advection into the Weddell Sea, leading to freshening at the surface. In the 400 ppm case, the tropical South Atlantic becomes saltier, which is likely due to a decrease in river runoff from

10 West Africa. However, the Weddell Sea becomes fresher in this case, due to a reduction of sinking in the South Atlantic and its associated salt advection.

Greenhouse warming enhances the hydrological cycle, due to the increased capacity of the atmosphere to hold water vapour. This effect is known as the Clausius-Clayperon relation. In the zonal mean, this

15 effect has been shown to create a pattern of change where wet regions get wetter and dry regions get drier. A simple scaling relation can be derived that relates the change (denoted by δ) in Precipitation minus Evaporation (P – E) to its original distribution (Held and Soden, 2006):

$$\delta(P - E) = \alpha \, \delta T \, (P - E),$$

where α is a constant and δT is the change in temperature. This scaling relation has been shown to hold

20 true over ocean regions in modern observations (Durack et al., 2012), but not over land where the dynamics of rainfall distribution are more complex (Greve et al., 2014). In line with the above scaling argument, the oceanic patterns of wet vs dry regions (Figure 3d) are enhanced in most ocean regions when CO_2 is doubled. The equatorial response of P-E has some exceptions to the scaling relation, as the western Pacific warm pool and equatorial cold tongue do not respond according to the same paradigm.

25 However, we note that the equatorial Pacific is subject to a strong zonal asymmetry due to El Nino variability, and these patterns do not follow the scaling relation as cleanly as the latitudinal relationship even in modern climate models (Held and Soden, 2006).

Climate
of the Past

Open Access

Discussions

EGU

The basin integrated forcing of P-E and river runoff upon the surface ocean is summarised in Figure 11. This illustrates the combined effects of P-E forcing and river runoff in creating much fresher Arctic conditions compared to present day. In comparing the control run (800 ppm) with the 1600 ppm and 400 ppm cases, the warmer simulations give rise to increased freshwater forcing in the North Pacific to

5   a similar degree as in the Arctic. However, the Arctic Ocean has a much smaller surface area and restricted outflow and therefore the impacts on surface salinity of this forcing are strongest. The connection of Arctic surface waters into the Atlantic gives rise to clear salinity changes in the North Atlantic, whereas the North Pacific salinity is less impacted by this change. Furthermore, the freshwater forcing is concentrated in the north-east of the basin, away from the deep water formation region in the

10 north-west. Thus the North Pacific is able to maintain deep water formation despite the enhanced freshwater forcing.

Overall, these changes in salinity are not enough to alter the preferred regions of northern sinking. The paleogeography employed here robustly generates sinking in the North Pacific and in the Southern

15 Ocean. In all cases, the northern cell is warmer and saltier, and the southern cell is colder and fresher and thus is heavier in the abyss, as in the present day. The cooling-induced weakening of the hydrological cycle does bring the North Atlantic closer to a regime of deep water formation, but these changes of 1-2 psu are not enough to trigger sinking. If we hypothesise that NADW did form at the EOT (Borrelli et al., 2014), then other mechanisms are needed to first raise the control state salinities in

20 the North Atlantic.

4.3 Meridional Overturning Circulation Response

Meridional overturning circulation is weaker in the 1600 ppm case, by around 10 Sv in the northern cell, and up to 15 Sv in the southern cell (Figure 12a). Although this is a substantial reduction, the overall structure remains similar to that seen in the control run (Figure 6), with sinking in the North

25 Pacific and Southern Ocean, albeit with a lower magnitude. The reduction in magnitude may be partly due to the lower CO_2 runs being further from equilibrium, and therefore the deep ocean is expelling more heat. Otherwise, the high CO_2 case has a lower meridional temperature gradient, which may

reduce the forcing of the MOC. In the 400 ppm case, the overall magnitude of the MOC is similar in magnitude to the control, however there is a northward shift of the southern cell, which manifests as a positive change in the high southern latitudes in Figure 12b. As the climate cools, a stable halocline develops in the Weddell Sea which ceases to form deep/bottom water. In winter, however, the halocline

5 supports the growth of seasonal sea ice in the region. Vigorous sinking occurs in the South Pacific in all cases, analogous to Ross Sea convection in the present day. This area is more predisposed to sinking due to a relative lack of river runoff ending up in that region, while the strong subpolar gyre circulation allows lower latitude water to maintain a salt feedback into the region.

4.4 Comparison with Biome Threshold

10 In order to investigate the implications of the climate sensitivity on vegetation, we have derived a model estimate of the palm/cycad line (Figure 13), which marks the coldest point where palms and cycad can survive. The palm/cycad line is a key indicator of the low seasonality during the Eocene, since it proves that frost-intolerant flora were able to exist at high latitudes (Huber and Caballero, 2011). Its associated equatorward movement indicates cooling and increased seasonality leading into the Oligocene (Eldrett

15 et al., 2009). Palm species have been estimated to require a cold month mean temperature (CMMT) of > 5°C, and a mean annual temperature (MAT) of > 10°C (Greenwood and Wing, 1995). In the control run (800 ppm), The MAT > 10°C threshold allows palms to exist as far north as 60°N across most longitudes. This includes the southern tip of Greenland, most of Europe and North America, while Siberia remains mostly too cold. The CMMT > 5°C criterion however is more restrictive, with the

20 cutoff moving further closer to 50°N at most longitudes. Nevertheless, the 1600 ppm simulation is warm enough to allow palms to exist far into the Arctic Circle, with the only exceptions being the interiors of Siberia and Greenland. In the Southern Hemisphere, Antarctica is virtually uninhabitable for palms due to the CMMT criterion, apart from the Antarctic Peninsula around 60-100°W. By contrast, all of Australia and virtually all of South America are warm enough to sustain palms even in the 400

25 ppm case.

The 1600 ppm palm/cycad lines indicate that the model can sustain some of the high latitude megathermal climate conditions typical of the Eocene, using CO_2 levels that agree with Eocene estimates (Anagnostou et al., 2016). We note that our model has a high sensitivity to CO_2 compared with recent Eocene modelling efforts (Huber and Caballero, 2011). While this helps to fit our model

5   with high latitude proxy estimates, we are still faced with the conundrum of being unable to fit low latitude temperature proxies simultaneously (see Figure 8).

5 Summary and Conclusion

This work presents a new configuration of the GFDL CM2.1 climate model, configured for the late Eocene. To our knowledge, the ~1° ocean resolution is the highest ocean resolution in a coupled model

10   of the late Eocene to date, while the lower resolution atmosphere ensures computational efficiency for long timescale simulations. This represents a significant step forward in resolution and accuracy in the representation of late Eocene paleogeography. Under this configuration, important gateways known to impact the ocean circulation at the EOT are better represented than has been done previously. The model shows relatively high sensitivity to CO_2 forcing, and a warm control climate under 800 ppm CO_2.

15   The model shows some agreement with SST proxies, although the model still does not capture the very low gradients from equator to pole implied by the available proxy records.

The model exhibits El Niño-like variability in the equatorial Pacific, though the western Pacific warm pool is larger and more persistent than present day. This creates a La Niña-like background state and

20   more robust east-west temperature difference. There are still major uncertainties and areas for future improvement in the model. These include possible improvements to the aerosols, vegetation, soil and river runoff schemes, which have been configured based on an opportunistic adaptation of available data. The sensitivity of these schemes has not been explored here, and may provide avenues for future improvement. For example, the contribution of land albedo, itself a function of vegetation and soil

25   properties, may have important impacts on both the land temperatures and the global meridional temperature gradient.

We find that the model robustly exhibits sinking in the North Pacific and the Southern Ocean, under all levels of CO_2. The southern water mass is colder and fresher and dominates the abyssal ocean, while the northern deep water mass is warmer and saltier, analogous to the present-day structure of North Atlantic Deep Water overlying Antarctic Bottom Water. The model is configured with a bottom roughness

5   mixing scheme and a uniform background diffusivity. Sensitivity tests indicate that using a Bryan-Lewis diffusivity scheme, commonly used in paleoclimate models, yields largely the same stratification and sinking regions. The Arctic Ocean is very fresh, with typical surface salinities of 20 psu, in agreement with Eocene salinity proxies. The connection between this freshwater mass and the North Atlantic prohibits the formation of North Atlantic Deep Water, even in the absence of tectonic barriers

10   in the Nordic Seas, since North Atlantic salinities are around 25-30 psu in present day sinking regions. These results highlight the importance of using late Eocene paleogeography in modelling the EOT. Using present day geography as a control state would not capture the dramatic differences in salinity in the northern ocean basins from the present day, which in turn greatly alter the preferred regions of sinking.

15

In response to CO_2 forcing, North Atlantic salinity responds clearly to a strengthening of the hydrological cycle under warming, and weakening under cooling. The net effect is a decrease of 1 psu in the North Atlantic for a doubling of CO_2, and an increase of 1-2 psu for a halving of CO_2. This effect is not enough to trigger North Atlantic sinking in the model. But it does suggest that if the climate were

20   closer to a North Atlantic sinking regime at the EOT due to factors not captured here, CO_2 cooling could provide a trigger. This model provides a platform for further sensitivity studies in altering aspects of the paleogeography. Changes to the Southern Ocean gateways, Arctic gateways, and the imposition of an ice sheet have all been shown to have significant impacts on the ocean circulation and climate in previous modelling studies. It is important to investigate such changes in a paleoclimate model with an

25   accurate representation of late Eocene paleogeography, so that changes across the EOT can be referenced to circulation, temperature and salinity characteristics that are appropriate to that time period.

Climate
of the Past
Discussions

References

Abelson, M. and Erez, J.: The onset of modern-like Atlantic meridional overturning circulation at the Eocene-Oligocene transition: Evidence, causes, and possible implications for global cooling,

10 Geochemistry, Geophys. Geosystems, 18(6), 2177–2199, doi:10.1002/2017GC006826, 2017.

Alexeev, V. A., Langen, P. L. and Bates, J. R.: Polar amplification of surface warming on an aquaplanet in "ghost forcing" experiments without sea ice feedbacks, Clim. Dyn., 24(7–8), 655–666, doi:10.1007/s00382-005-0018-3, 2005.

Anagnostou, E., John, E. H., Edgar, K. M., Foster, G. L., Ridgwell, A., Inglis, G. N., Pancost, R. D.,

15 Lunt, D. J. and Pearson, P. N.: Changing atmospheric CO2 concentration was the primary driver of early Cenozoic climate, Nature, 533(7603), 380–384, 2016.

Baatsen, M., van Hinsbergen, D. J. J., von der Heydt, A. S., Dijkstra, H. A., Sluijs, A., Abels, H. A. and Bijl, P. K.: Reconstructing geographical boundary conditions for palaeoclimate modelling during the Cenozoic, Clim. Past, 12(8), 1635–1644, doi:10.5194/cp-12-1635-2016, 2016.

20 Barker, P. F., Filippelli, G. M., Florindo, F., Martin, E. E. and Scher, H. D.: Onset and role of the Antarctic Circumpolar Current, Deep Sea Res. Part II Top. Stud. Oceanogr., 54(21–22), 2388–2398, doi:10.1016/j.dsr2.2007.07.028, 2007.

Bijl, P. K., Schouten, S., Sluijs, A., Reichart, G.-J., Zachos, J. C. and Brinkhuis, H.: Early Palaeogene temperature evolution of the southwest Pacific Ocean, Nature, 461(7265), 776–779, 2009.

25 de Boer, A. M. and Hogg, A. M.: Control of the glacial carbon budget by topographically induced mixing, Geophys. Res. Lett., 41(12), 4277–4284, doi:10.1002/2014GL059963, 2014.

Climate
of the Past
Discussions

Open Access

EGU

Bohaty, S. M., Zachos, J. C. and Delaney, M. L.: Foraminiferal Mg/Ca evidence for Southern Ocean cooling across the Eocene–Oligocene transition, Earth Planet. Sci. Lett., 317–318(Supplement C), 251–261, doi:https://doi.org/10.1016/j.epsl.2011.11.037, 2012.

Borrelli, C., Cramer, B. S. and Katz, M. E.: Bipolar Atlantic deepwater circulation in the middle-late

5   Eocene: Effects of Southern Ocean gateway openings, Paleoceanography, 29(4), 308–327, doi:10.1002/2012PA002444, 2014.

Cox, M. D.: An Idealized Model of the World Ocean. Part I: The Global-Scale Water Masses, J. Phys. Oceanogr., 19(11), 1730–1752, doi:10.1175/1520-0485(1989)019<1730:AIMOTW>2.0.CO;2, 1989.

Coxall, H. K. and Pearson, P. N.: The Eocene-Oligocene transition, Deep Time Perspect. Clim. Chang.

10   Marrying Signal From Comput. Model. Biol. Proxies, 351–387, 2007.

Coxall, H. K., Wilson, P. A., Palike, H., Lear, C. H. and Backman, J.: Rapid stepwise onset of Antarctic glaciation and deeper calcite compensation in the Pacific Ocean, Nature, 433(7021), 53–57, doi:10.1038/nature03135, 2005.

Cramer, B. S., Toggweiler, J. R., Wright, J. D., Katz, M. E. and Miller, K. G.: Ocean overturning since

15   the Late Cretaceous: Inferences from a new benthic foraminiferal isotope compilation, Paleoceanography, 24(4), PA4216, doi:10.1029/2008PA001683, 2009.

Danabasoglu, G., McWilliams, J. C. and Large, W. G.: Approach to Equilibrium in Accelerated Global Oceanic Models, J. Clim., 9(5), 1092–1110, doi:10.1175/1520-0442(1996)009<1092:ATEIAG>2.0.CO;2, 1996.

20   DeConto, R. M. and Pollard, D.: Rapid Cenozoic glaciation of Antarctica induced by declining atmospheric CO2, Nature, 421(6920), 245–249, doi:10.1038/nature01290, 2003.

Delworth, T. L., Broccoli, A. J., Rosati, A., Stouffer, R. J., Balaji, V., Beesley, J. A., Cooke, W. F., Dixon, K. W., Dunne, J., Dunne, K. A., Durachta, J. W., Findell, K. L., Ginoux, P., Gnanadesikan, A., Gordon, C. T., Griffies, S. M., Gudgel, R., Harrison, M. J., Held, I. M., Hemler, R. S., Horowitz, L. W.,

25   Klein, S. A., Knutson, T. R., Kushner, P. J., Langenhorst, A. R., Lee, H.-C., Lin, S.-J., Lu, J., Malyshev, S. L., Milly, P. C. D., Ramaswamy, V., Russell, J., Schwarzkopf, M. D., Shevliakova, E., Sirutis, J. J., Spelman, M. J., Stern, W. F., Winton, M., Wittenberg, A. T., Wyman, B., Zeng, F. and Zhang, R.: GFDL's CM2 Global Coupled Climate Models. Part I: Formulation and Simulation Characteristics, J.

Clim., 19(5), 643–674, doi:10.1175/JCLI3629.1, 2006.

Delworth, T. L., Rosati, A., Anderson, W., Adcroft, A. J., Balaji, V., Benson, R., Dixon, K., Griffies, S. M., Lee, H.-C., Pacanowski, R. C., Vecchi, G. A., Wittenberg, A. T., Zeng, F. and Zhang, R.: Simulated Climate and Climate Change in the GFDL CM2.5 High-Resolution Coupled Climate Model, J. Clim., 25(8), 2755–2781, doi:10.1175/JCLI-D-11-00316.1, 2012.

Dupont-Nivet, G., Krijgsman, W., Langereis, C. G., Abels, H. A., Dai, S. and Fang, X.: Tibetan plateau aridification linked to global cooling at the Eocene–Oligocene transition, Nature, 445, 635, 2007.

Durack, P. J., Wijffels, S. E. and Matear, R. J.: Ocean Salinities Reveal Strong Global Water Cycle Intensification During 1950 to 2000, Science, 336(6080), 455–458, doi:10.1126/science.1212222, 2012.

Eldrett, J. S., Greenwood, D. R., Harding, I. C. and Huber, M.: Increased seasonality through the Eocene to Oligocene transition in northern high latitudes, Nature, 459(7249), 969–973, 2009.

Elsworth, G., Galbraith, E., Halverson, G. and Yang, S.: Enhanced weathering and CO_2 drawdown caused by latest Eocene strengthening of the Atlantic meridional overturning circulation, Nat. Geosci, 10(3), 213–216, 2017.

England, M. H., Hutchinson, D. K., Santoso, A. and Sijp, W. P.: Ice–Atmosphere Feedbacks Dominate the Response of the Climate System to Drake Passage Closure, J. Clim., 30(15), 5775–5790, doi:10.1175/JCLI-D-15-0554.1, 2017.

Ferreira, D., Cessi, P., Coxall, H. K., Boer, A. de, Dijkstra, H. A., Drijfhout, S. S., Eldevik, T., Harnik, N., McManus, J. F., Marshall, D. P., Nilsson, J., Roquet, F., Schneider, T. and Wills, R. C.: Atlantic-Pacific asymmetry in deep water formation, Annu. Rev. Earth Planet. Sci., in press, 2018.

Fyke, J. G., D'Orgeville, M. and Weaver, A. J.: Drake Passage and Central American Seaway controls on the distribution of the oceanic carbon reservoir, Glob. Planet. Change, 128(0), 72–82, doi:10.1016/j.gloplacha.2015.02.011, 2015.

Galbraith, E. D., Gnanadesikan, A., Dunne, J. P. and Hiscock, M. R.: Regional impacts of iron-light colimitation in a global biogeochemical model, Biogeosciences, 7(3), 1043–1064, doi:10.5194/bg-7-1043-2010, 2010.

Gasson, E., Lunt, D. J., DeConto, R., Goldner, A., Heinemann, M., Huber, M., LeGrande, A. N., Pollard, D., Sagoo, N., Siddall, M., Winguth, A. and Valdes, P. J.: Uncertainties in the modelled CO_2

threshold for Antarctic glaciation, Clim. Past, 10(2), 451–466, doi:10.5194/cp-10-451-2014, 2014.

Goldner, A., Huber, M. and Caballero, R.: Does Antarctic glaciation cool the world?, Clim. Past, 9, 173–189, doi:10.5194/cp-9-173-2013, 2013.

Goldner, A., Herold, N. and Huber, M.: Antarctic glaciation caused ocean circulation changes at the

5 Eocene-Oligocene transition, Nature, 511(7511), 574–577, doi:10.1038/nature13597, 2014.

Gomes Rodrigues, H., Marivaux, L. and Vianey-Liaud, M.: Expansion of open landscapes in Northern China during the Oligocene induced by dramatic climate changes: Paleoecological evidence, Palaeogeogr. Palaeoclimatol. Palaeoecol., 358–360(Supplement C), 62–71, doi:https://doi.org/10.1016/j.palaeo.2012.07.025, 2012.

10 Greenwood, D. R. and Wing, S. L.: Eocene continental climates and latitudinal temperature gradients, Geology, 23(11), 1044–1048, doi:10.1130/0091-7613(1995)023<1044:ECCALT>2.3.CO;2, 1995.

Greve, P., Orlowsky, B., Mueller, B., Sheffield, J., Reichstein, M. and Seneviratne, S. I.: Global assessment of trends in wetting and drying over land, Nat. Geosci., 7, 716, 2014.

Griffies, S. M., Biastoch, A., Böning, C., Bryan, F., Danabasoglu, G., Chassignet, E. P., England, M.

15 H., Gerdes, R., Haak, H., Hallberg, R. W., Hazeleger, W., Jungclaus, J., Large, W. G., Madec, G., Pirani, A., Samuels, B. L., Scheinert, M., Gupta, A. Sen, Severijns, C. A., Simmons, H. L., Treguier, A. M., Winton, M., Yeager, S. and Yin, J.: Coordinated Ocean-ice Reference Experiments (COREs), Ocean Model., 26(1–2), 1–46, doi:10.1016/j.ocemod.2008.08.007, 2009.

Held, I. M. and Soden, B. J.: Robust responses of the hydrological cycle to global warming, J. Clim.,

20 19(21), 5686–5699, doi:10.1175/JCLI3990.1, 2006.

Herold, N., Buzan, J., Seton, M., Goldner, A., Green, J. A. M., Müller, R. D., Markwick, P. and Huber, M.: A suite of early Eocene (~ 55 Ma) climate model boundary conditions, Geosci. Model Dev., 7(5), 2077–2090, doi:10.5194/gmd-7-2077-2014, 2014.

von der Heydt, A. and Dijkstra, H. A.: Effect of ocean gateways on the global ocean circulation in the

25 late Oligocene and early Miocene, Paleoceanography, 21(1), PA1011, doi:10.1029/2005PA001149, 2006.

van Hinsbergen, D. J. J., de Groot, L. V, van Schaik, S. J., Spakman, W., Bijl, P. K., Sluijs, A., Langereis, C. G. and Brinkhuis, H.: A Paleolatitude Calculator for Paleoclimate Studies., PLoS One,

10(6), e0126946, doi:10.1371/journal.pone.0126946, 2015.

Huber, M. and Caballero, R.: The early Eocene equable climate problem revisited, Clim. Past, 7(2), 603–633, doi:10.5194/cp-7-603-2011, 2011.

Hutchinson, D. K., England, M. H., Hogg, A. M. and Snow, K.: Interhemispheric Asymmetry of
5   Warming in an Eddy-Permitting Coupled Sector Model, J. Clim., 28(18), 7385–7406, doi:10.1175/JCLI-D-15-0014.1, 2015.

Kennedy, A. T., Farnsworth, A., Lunt, D. J., Lear, C. H. and Markwick, P. J.: Atmospheric and oceanic impacts of Antarctic glaciation across the Eocene–Oligocene transition, Phil. Trans. R. Soc. A, 373(2054), 20140419, doi:10.1098/rsta.2014.0419, 2015.

10 Kennett, J. P.: Cenozoic Evolution of Antarctic Glaciation, the Circum-Antarctic Ocean, and Their Impact on Global Paleoceanography, J. Geophys. Res., 82(27), 3843–3860, doi:10.1029/JC082i027p03843, 1977.

Kim, J.-H., van der Meer, J., Schouten, S., Helmke, P., Willmott, V., Sangiorgi, F., Koç, N., Hopmans, E. C. and Damsté, J. S. S.: New indices and calibrations derived from the distribution of crenarchaeal
15 isoprenoid tetraether lipids: Implications for past sea surface temperature reconstructions, Geochim. Cosmochim. Acta, 74(16), 4639–4654, doi:http://dx.doi.org/10.1016/j.gca.2010.05.027, 2010.

Kirtman, B. P., Bitz, C., Bryan, F., Collins, W., Dennis, J., Hearn, N., Kinter, J. L., Loft, R., Rousset, C., Siqueira, L., Stan, C., Tomas, R. and Vertenstein, M.: Impact of ocean model resolution on CCSM climate simulations, Clim. Dyn., 39(6), 1303–1328, doi:10.1007/s00382-012-1500-3, 2012.

20 Ladant, J.-B., Donnadieu, Y., Lefebvre, V. and Dumas, C.: The respective role of atmospheric carbon dioxide and orbital parameters on ice sheet evolution at the Eocene-Oligocene transition, Paleoceanography, 29(8), 810–823, doi:10.1002/2013PA002593, 2014.

Lefebvre, V., Donnadieu, Y., Sepulchre, P., Swingedouw, D. and Zhang, Z.-S.: Deciphering the role of southern gateways and carbon dioxide on the onset of the Antarctic Circumpolar Current,
25 Paleoceanography, 27(4), PA4201, doi:10.1029/2012PA002345, 2012.

Liu, Z., Pagani, M., Zinniker, D., DeConto, R., Huber, M., Brinkhuis, H., Shah, S. R., Leckie, R. M. and Pearson, A.: Global Cooling During the Eocene-Oligocene Climate Transition, Science, 323(5918), 1187–1190, doi:10.1126/science.1166368, 2009.

Livermore, R., Nankivell, A., Eagles, G. and Morris, P.: Paleogene opening of Drake Passage, Earth Planet. Sci. Lett., 236(1–2), 459–470, doi:http://dx.doi.org/10.1016/j.epsl.2005.03.027, 2005.

Locarnini, R. A., Mishonov, A. V, Antonov, J. I., Boyer, T. P., Garcia, H. E., Baranova, O. K., Zweng, M. M., Paver, C. R., Reagan, J. R., Johnson, D. R., Hamilton, M. and D., S.: World Ocean Atlas 2013, Volume 1: Temperature, 2013.

Lunt, D. J., Dunkley Jones, T., Heinemann, M., Huber, M., LeGrande, A., Winguth, A., Loptson, C., Marotzke, J., Roberts, C. D., Tindall, J., Valdes, P. and Winguth, C.: A model–data comparison for a multi-model ensemble of early Eocene atmosphere–ocean simulations: EoMIP, Clim. Past, 8(5), 1717–1736, doi:10.5194/cp-8-1717-2012, 2012.

Lunt, D. J., Farnsworth, A., Loptson, C., Foster, G. L., Markwick, P., O'Brien, C. L., Pancost, R. D., Robinson, S. A. and Wrobel, N.: Palaeogeographic controls on climate and proxy interpretation, Clim. Past, 12(5), 1181–1198, doi:10.5194/cp-12-1181-2016, 2016.

Lunt, D. J., Huber, M., Anagnostou, E., Baatsen, M. L. J., Caballero, R., DeConto, R., Dijkstra, H. A., Donnadieu, Y., Evans, D., Feng, R., Foster, G. L., Gasson, E., von der Heydt, A. S., Hollis, C. J., Inglis, G. N., Jones, S. M., Kiehl, J., Kirtland Turner, S., Korty, R. L., Kozdon, R., Krishnan, S., Ladant, J.-B., Langebroek, P., Lear, C. H., LeGrande, A. N., Littler, K., Markwick, P., Otto-Bliesner, B., Pearson, P., Poulsen, C. J., Salzmann, U., Shields, C., Snell, K., Stärz, M., Super, J., Tabor, C., Tierney, J. E., Tourte, G. J. L., Tripati, A., Upchurch, G. R., Wade, B. S., Wing, S. L., Winguth, A. M. E., Wright, N. M., Zachos, J. C. and Zeebe, R. E.: The DeepMIP contribution to PMIP4: experimental design for model simulations of the EECO, PETM, and pre-PETM (version 1.0), Geosci. Model Dev., 10(2), 889–901, doi:10.5194/gmd-10-889-2017, 2017.

Maffre, P., Ladant, J.-B., Donnadieu, Y., Sepulchre, P. and Goddéris, Y.: The influence of orography on modern ocean circulation, Clim. Dyn., 1–13, doi:10.1007/s00382-017-3683-0, 2017.

Miller, K. G., Wright, J. D. and Fairbanks, R. G.: Unlocking the Ice House: Oligocene-Miocene oxygen isotopes, eustasy, and margin erosion, J. Geophys. Res. Solid Earth, 96(B4), 6829–6848, doi:10.1029/90JB02015, 1991.

Murray, R. J.: Explicit Generation of Orthogonal Grids for Ocean Models, J. Comput. Phys., 126(2), 251–273, doi:10.1006/jcph.1996.0136, 1996.

28

Nycander, J., Hieronymus, M. and Roquet, F.: The nonlinear equation of state of sea water and the global water mass distribution, Geophys. Res. Lett., 42(18), 7714–7721, doi:10.1002/2015GL065525, 2015.

Pearson, P. N., van Dongen, B. E., Nicholas, C. J., Pancost, R. D., Schouten, S., Singano, J. M. and
5 Wade, B. S.: Stable warm tropical climate through the Eocene Epoch, Geology, 35(3), 211–214, 2007.

Pearson, P. N., Foster, G. L. and Wade, B. S.: Atmospheric carbon dioxide through the Eocene–Oligocene climate transition, Nature, 461(7267), 1110–1113, 2009.

Sewall, J. O., Sloan, L. C., Huber, M. and Wing, S.: Climate sensitivity to changes in land surface characteristics, Glob. Planet. Change, 26(4), 445–465, doi:http://dx.doi.org/10.1016/S0921-
10 8181(00)00056-4, 2000.

Sijp, W. P. and England, M. H.: Effect of the Drake Passage Throughflow on Global Climate, J. Phys. Oceanogr., 34(5), 1254–1266, doi:10.1175/1520-0485(2004)034<1254:EOTDPT>2.0.CO;2, 2004.

Sijp, W. P., England, M. H. and Toggweiler, J. R.: Effect of Ocean Gateway Changes under Greenhouse Warmth, J. Clim., 22(24), 6639–6652, doi:10.1175/2009JCLI3003.1, 2009.

15 Sijp, W. P., England, M. H. and Huber, M.: Effect of the deepening of the Tasman Gateway on the global ocean, Paleoceanography, 26(4), PA4207, doi:10.1029/2011PA002143, 2011.

Sijp, W. P., von der Heydt, A. S., Dijkstra, H. A., Flögel, S., Douglas, P. M. J. and Bijl, P. K.: The role of ocean gateways on cooling climate on long time scales, Glob. Planet. Change, 119(0), 1–22, doi:10.1016/j.gloplacha.2014.04.004, 2014.

20 Simmons, H. L., Jayne, S. R., Laurent, L. C. S. and Weaver, A. J.: Tidally driven mixing in a numerical model of the ocean general circulation, Ocean Model., 6(3–4), 245–263, doi:10.1016/S1463-5003(03)00011-8, 2004.

Sinha, B., Blaker, A. T., Hirschi, J. J.-M., Bonham, S., Brand, M., Josey, S., Smith, R. S. and Marotzke, J.: Mountain ranges favour vigorous Atlantic meridional overturning, Geophys. Res. Lett., 39(2),
25 L02705, doi:10.1029/2011GL050485, 2012.

Stickley, C. E., Brinkhuis, H., Schellenberg, S. A., Sluijs, A., Röhl, U., Fuller, M., Grauert, M., Huber, M., Warnaar, J. and Williams, G. L.: Timing and nature of the deepening of the Tasmanian Gateway, Paleoceanography, 19(4), PA4027, doi:10.1029/2004PA001022, 2004.

29

Stickley, C. E., St John, K., Koç, N., Jordan, R. W., Passchier, S., Pearce, R. B. and Kearns, L. E.: Evidence for middle Eocene Arctic sea ice from diatoms and ice-rafted debris, Nature, 460, 376, 2009.

Thomas, D. J., Korty, R., Huber, M., Schubert, J. A. and Haines, B.: Nd isotopic structure of the Pacific Ocean 70-30 Ma and numerical evidence for vigorous ocean circulation and ocean heat transport in a

5   greenhouse world, Paleoceanography, 29(5), 454–469, doi:10.1002/2013PA002535, 2014.

Thorn, V. C. and DeConto, R.: Antarctic climate at the Eocene/Oligocene boundary — climate model sensitivity to high latitude vegetation type and comparisons with the palaeobotanical record, Palaeogeogr.   Palaeoclimatol.   Palaeoecol.,   231(1),   134–157, doi:https://doi.org/10.1016/j.palaeo.2005.07.032, 2006.

10   Toggweiler, J. R. and Samuels, B.: Effect of drake passage on the global thermohaline circulation, Deep Sea Res. Part I Oceanogr. Res. Pap., 42(4), 477–500, 1995.

Torsvik, T. H., Van der Voo, R., Preeden, U., Mac Niocaill, C., Steinberger, B., Doubrovine, P. V, van Hinsbergen, D. J. J., Domeier, M., Gaina, C., Tohver, E., Meert, J. G., McCausland, P. J. A. and Cocks, L. R. M.: Phanerozoic polar wander, palaeogeography and dynamics, Earth-Science Rev., 114(3), 325–

15   368, doi:http://dx.doi.org/10.1016/j.earscirev.2012.06.007, 2012.

Utescher, T. and Mosbrugger, V.: Eocene vegetation patterns reconstructed from plant diversity — A global   perspective,   Palaeogeogr.   Palaeoclimatol.   Palaeoecol.,   247(3),   243–271, doi:https://doi.org/10.1016/j.palaeo.2006.10.022, 2007.

Viebahn, J. P., von der Heydt, A. S., Le Bars, D. and Dijkstra, H. A.: Effects of Drake Passage on a

20   strongly eddying global ocean, Paleoceanography, 31(5), 564–581, doi:10.1002/2015PA002888, 2016.

Warren, B. A.: Why is no deep water formed in the North Pacific?, J. Mar. Res., 41(2), 327–347, doi:10.1357/002224083788520207, 1983.

Wills, R. C. and Schneider, T.: Stationary Eddies and the Zonal Asymmetry of Net Precipitation and Ocean Freshwater Forcing, J. Clim., 28(13), 5115–5133, doi:10.1175/JCLI-D-14-00573.1, 2015.

25   Winton, M., Takahashi, K. and Held, I. M.: Importance of Ocean Heat Uptake Efficacy to Transient Climate Change, J. Clim., 23(9), 2333–2344, doi:10.1175/2009JCLI3139.1, 2010.

Wolfe, C. L. and Cessi, P.: Salt Feedback in the Adiabatic Overturning Circulation, J. Phys. Oceanogr., 44(4), 1175–1194, doi:10.1175/JPO-D-13-0154.1, 2014.

Yang, S., Galbraith, E. and Palter, J.: Coupled climate impacts of the Drake Passage and the Panama
Seaway, Clim. Dyn., 43(1–2), 37–52, doi:10.1007/s00382-013-1809-6, 2014.

Zhang, Z.-S., Yan, Q. and Wang, H.-J.: Has the Drake Passage Played an Essential Role in the
Cenozoic Cooling?, Atmos. Ocean. Sci. Lett., 3(5), 288–292, 2010.

5

Climate
of the Past
Discussions
Open Access

List of Figures

15

Climate
of the Past
Discussions

Open Access

EGU

Figure 1: Bathymetry and topography of the late Eocene, adapted from (Baatsen et al., 2016). Both figures are plotted using a cell fill method, illustrating the resolution of the grid cells in each case. Due to the difference in resolution between the ocean and atmosphere, coastal grid cells in the atmosphere typically contain a fraction of both land and ocean.

5

Climate
of the Past

Discussions

Open Access
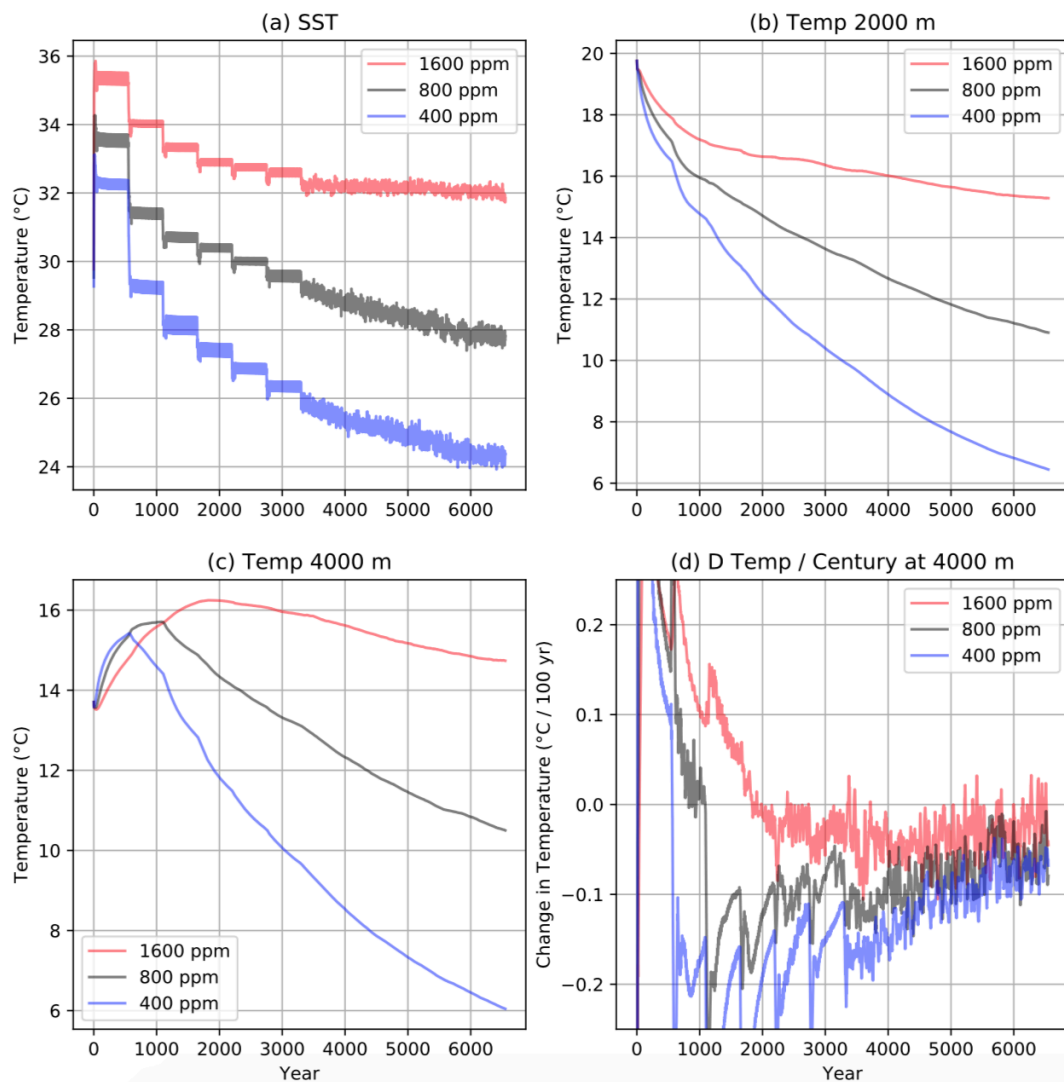
Figure 2: Spinup evolution of the 400, 800 and 1600 ppm simulations, showing the global mean temperature evolution at (a) the surface, (b) 2000 m, (c) 4000 m and (d) the time rate of change at 4000 m. (d) is filtered using a 9-year running mean.

5

Climate
of the Past
Discussions
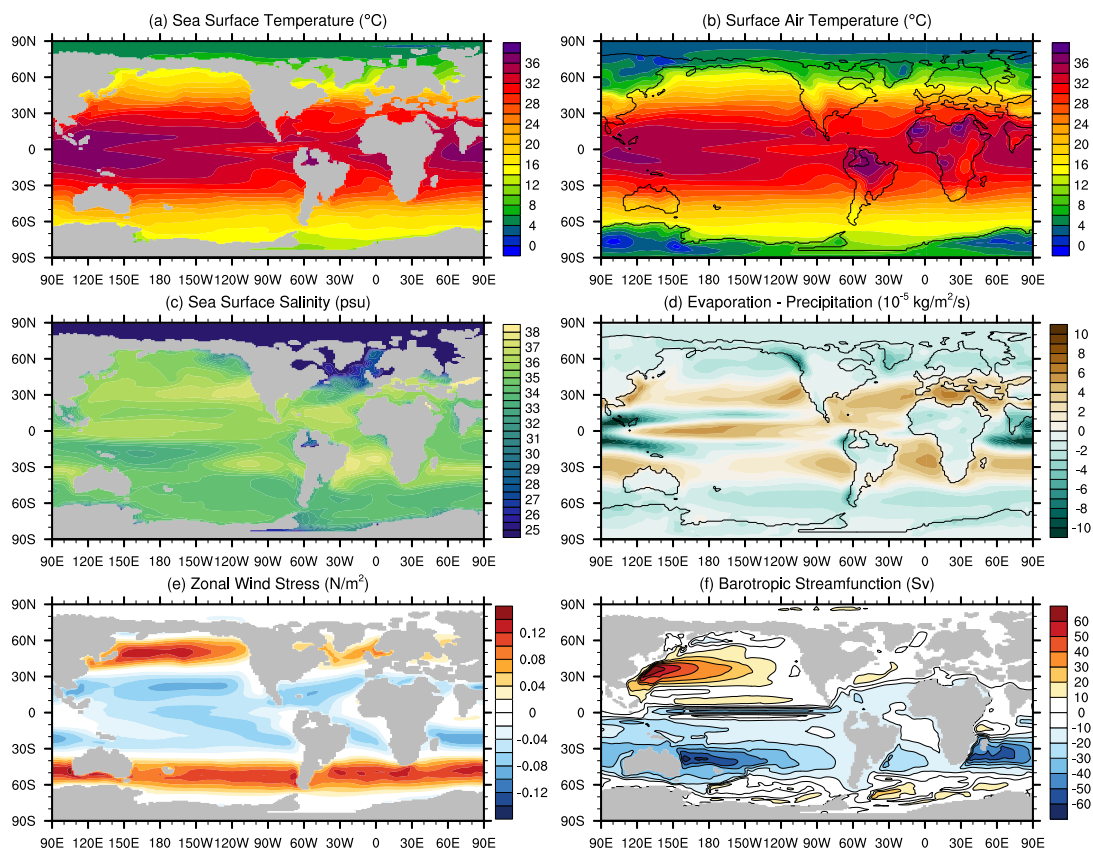
Figure 3: Control climate state for our 38 Ma model, showing (a) sea surface temperature (SST), (b) surface air temperature (SAT), (c) sea surface salinity (SSS), (d) evaporation minus precipitation, (e) barotropic streamfunction and (f) zonal wind stress.

5

36

Climate
of the Past
Discussions
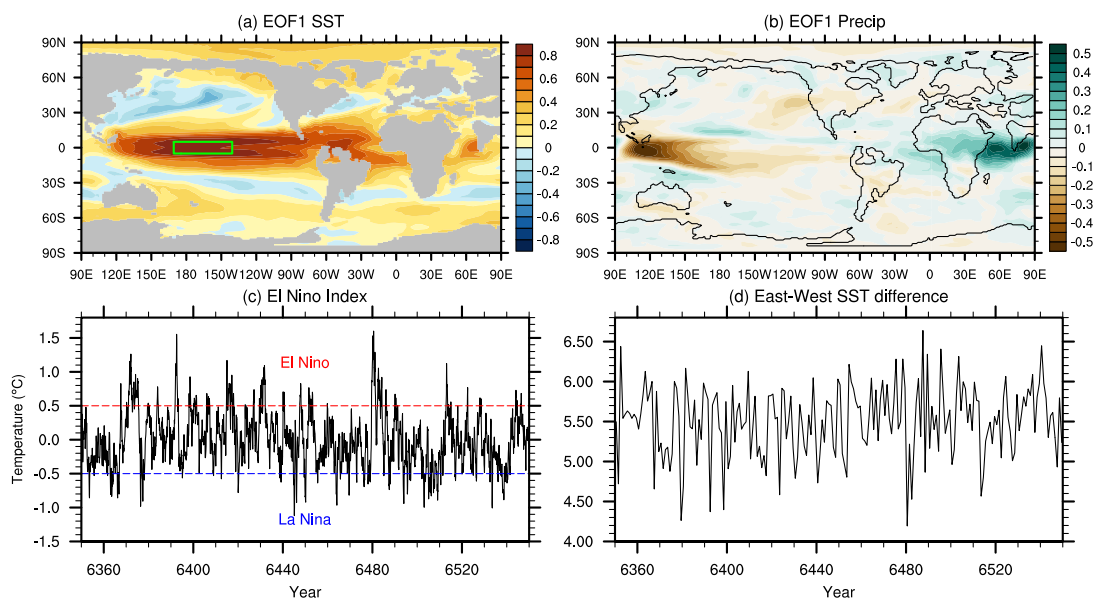
Figure 4: (a) 1ˢᵗ Empirical Orthogonal Function (EOF1) of monthly sea surface temperature anomaly (SST), and (b) precipitation. From the EOF1 of SST we then define an El Niño index region from 170°E to 140°W, and from 5°S to 5°N, as shown in the green box in (a). This region was chosen as an 'El Niño index' to be representative of strongest variability in Pacific SST. (c) El Niño index variability in monthly SST anomaly. (d) Annual mean east-west Pacific SST difference.
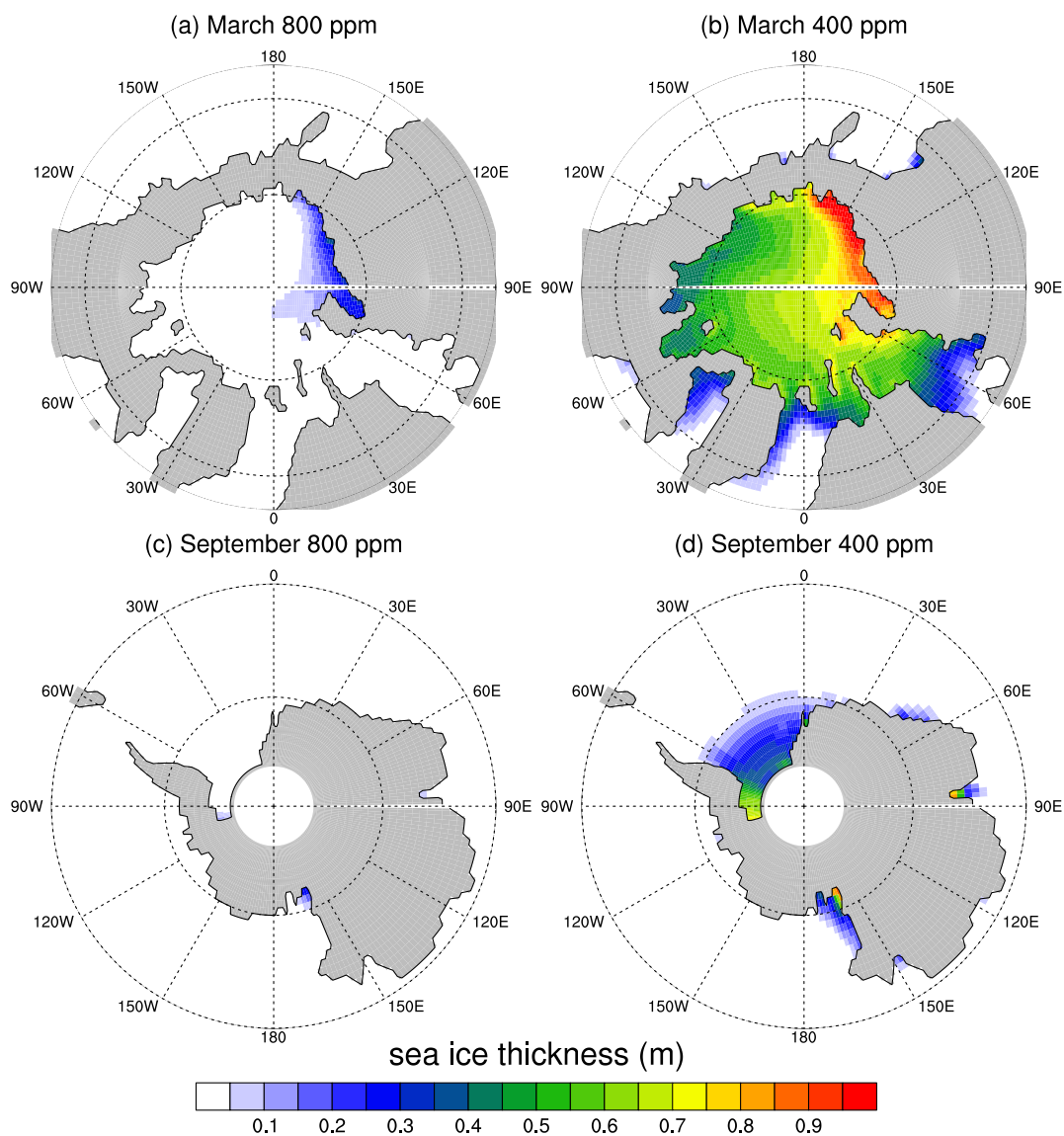
Figure 5: March (NH maximum) sea ice thickness of (a) the 800 ppm run, and (b) the 400 ppm run, and September (SH maximum) sea ice thickness for the (c) 800 ppm run and the (d) 400 ppm run. The 1600 ppm run is sea ice free all year.
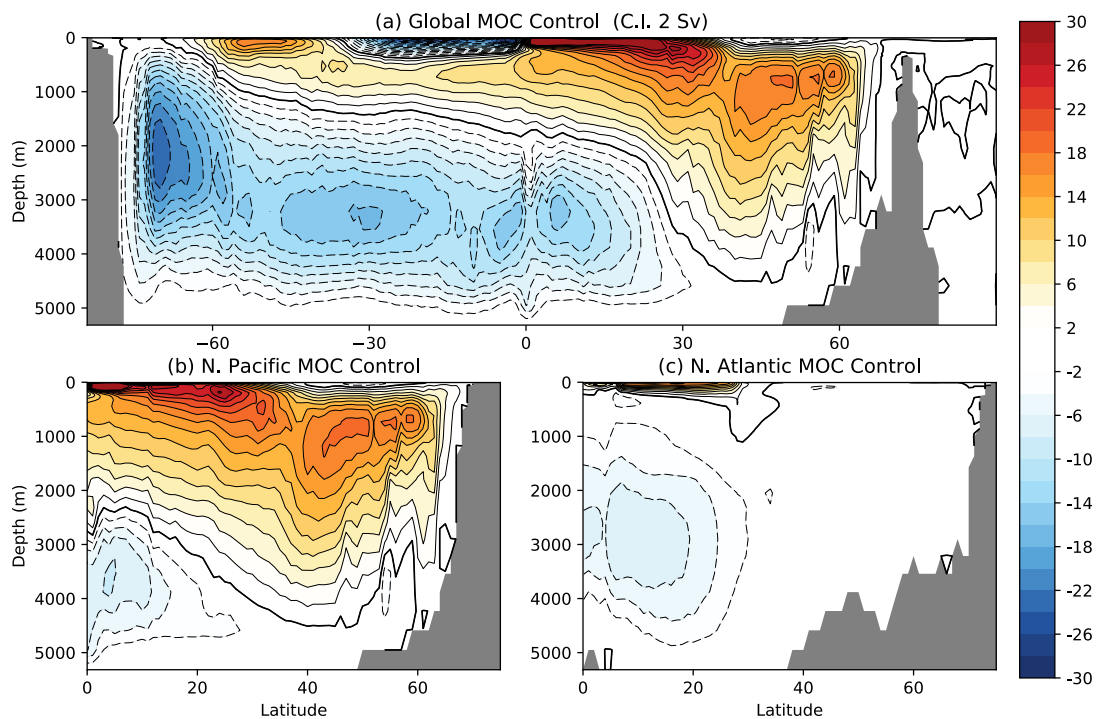
Figure 6: (a) Global Meridional Overturning Circulation (MOC), with the northern hemisphere MOC split into (b) Pacific basin and (c) Atlantic basin.
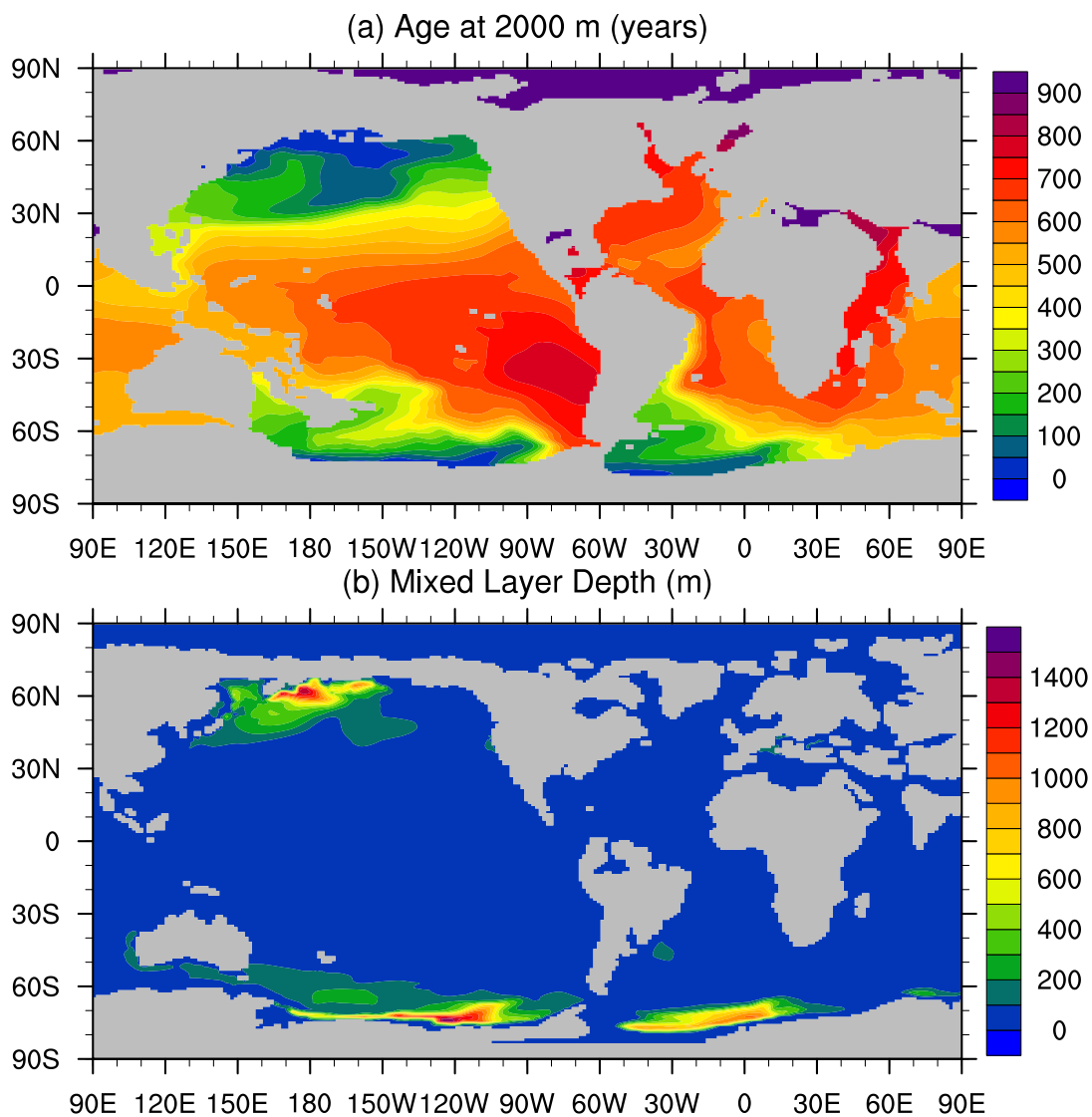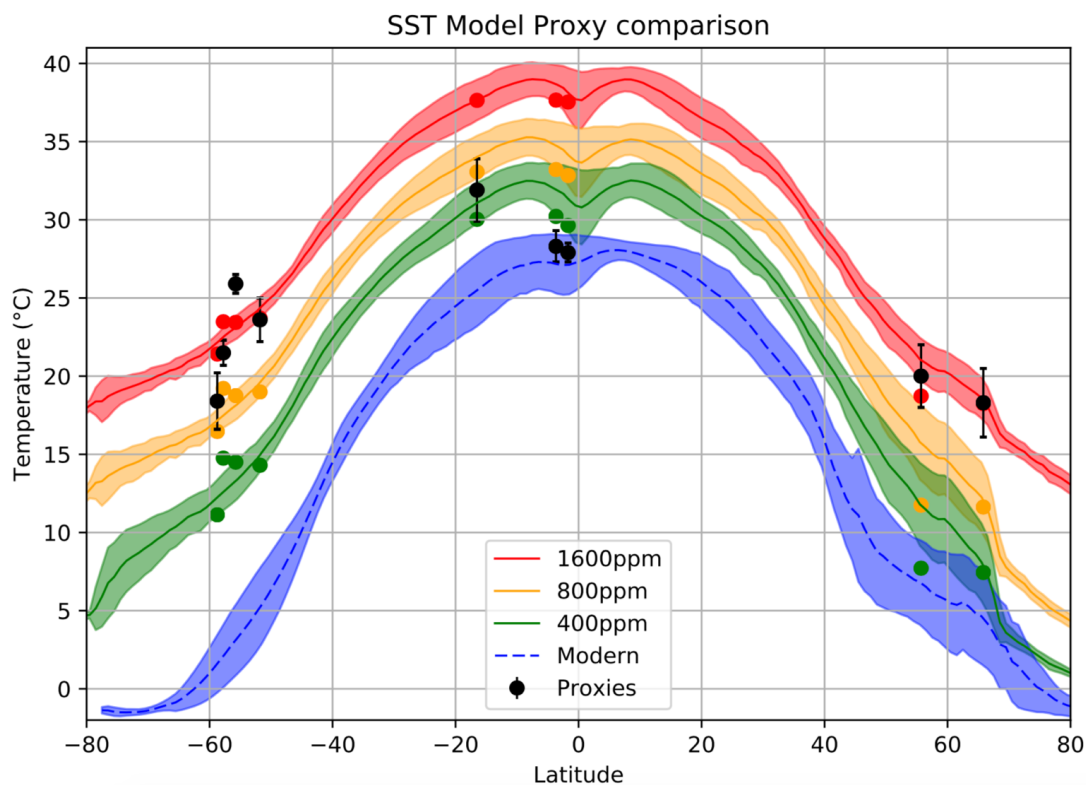
Figure 7: (a) Age tracer at 2000 m depth and (b) mixed layer depth. Note that the age scale is saturated in the Arctic, where the strong halocline prevents ventilation and ages are greater than 3000 years.

Figure 8: Comparison of model 1600 ppm (red), 800 ppm (orange) and 400 ppm (green) simulations with a compilation of SST proxy data (black circles), combining UK'$_{37}$, TEX$_{86}$ and Mg/Ca data (Bijl et al., 2009; Liu et al., 2009; Pearson et al., 2007). The model temperature for each proxy location is shown by the coloured circles. The zonal mean and standard deviation are shown by the solid lines and shaded areas respectively. Also shown in blue is an equivalent distribution of zonal mean and standard deviation from the modern World Ocean Atlas (Locarnini et al., 2013).
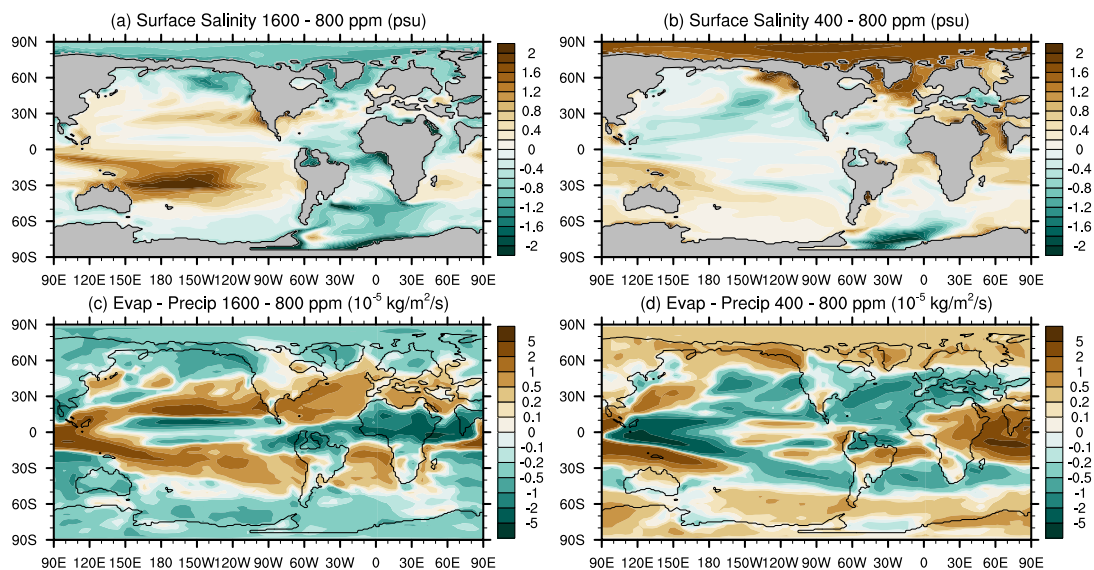
Climate
of the Past
Discussions

Open Access

EGU
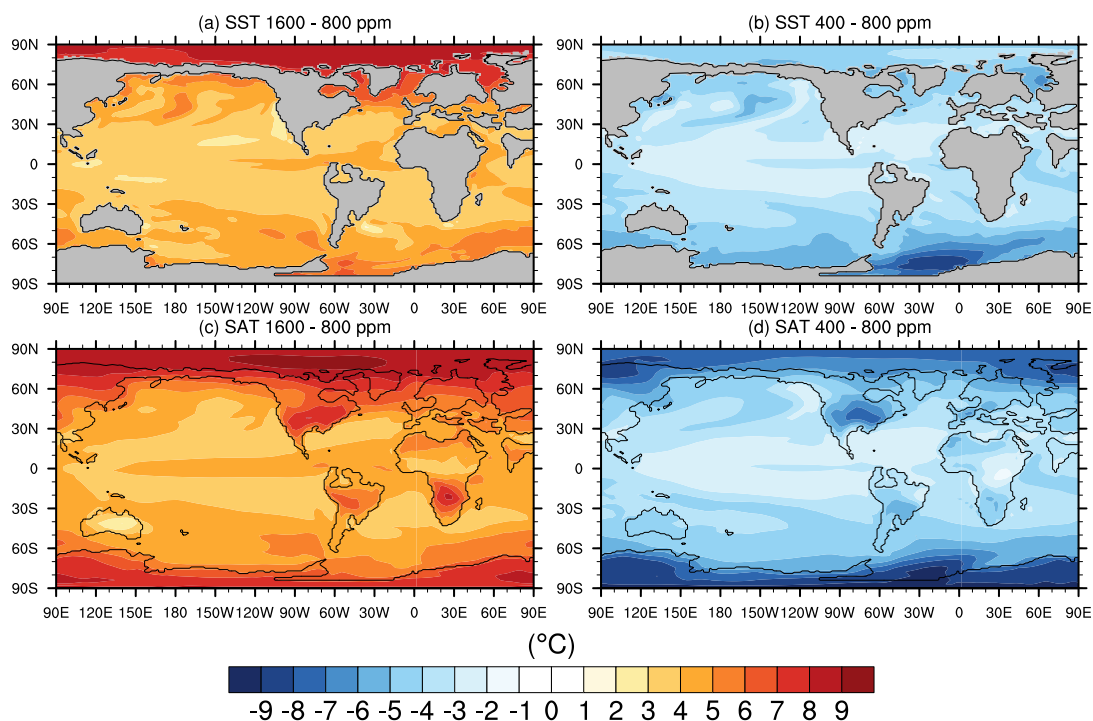
Figure 9: Sea surface temperature (SST) response to (a) doubling and (b) halving CO_2, and surface air temperature response (SAT) to (c) doubling and (d) halving CO_2.

Figure 10: Salinity changes in response to (a) doubling and (b) halving CO_2, with the corresponding changes in evaporation minus precipitation for (c) doubling and (d) halving CO_2. Note the non-linear scale in plots (c-d).
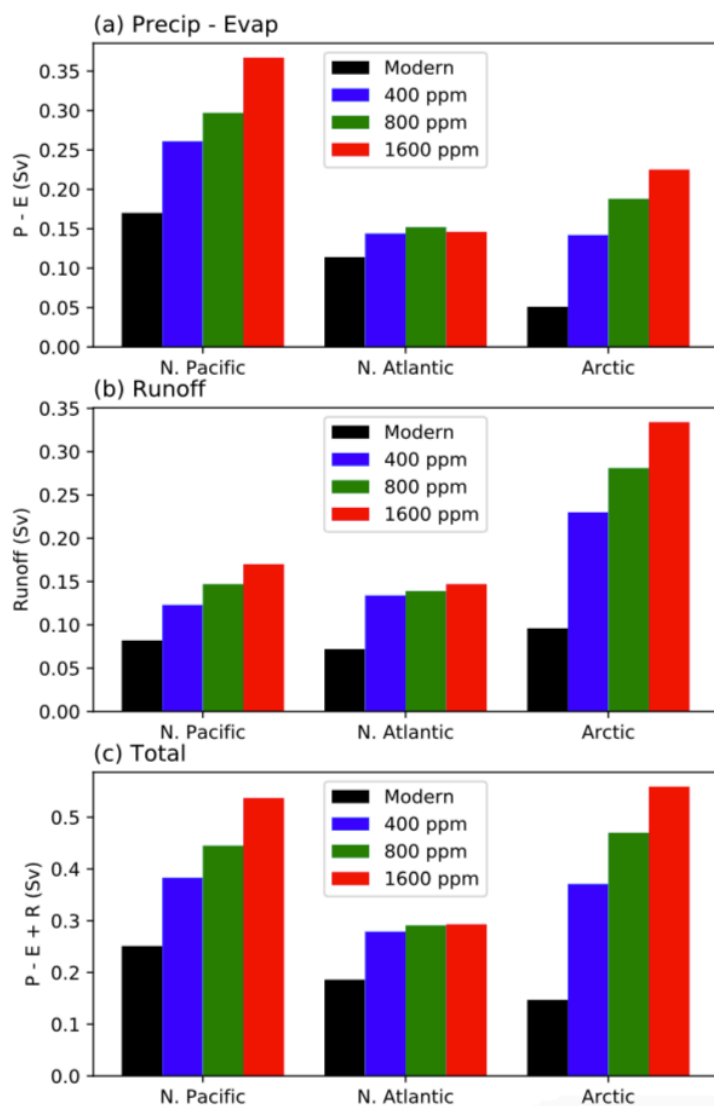
43

Figure 11: (a) Precipitation – evaporation into the North Pacific and North Atlantic (both with a cutoff latitude of 45°N) and the Arctic Ocean, comparing a modern CM2.1 simulation with the late Eocene model at 400, 800 and 1600 ppm. (b) shows river runoff with the same breakdown as in (a), while (c) shows the total of precipitation – evaporation plus runoff.
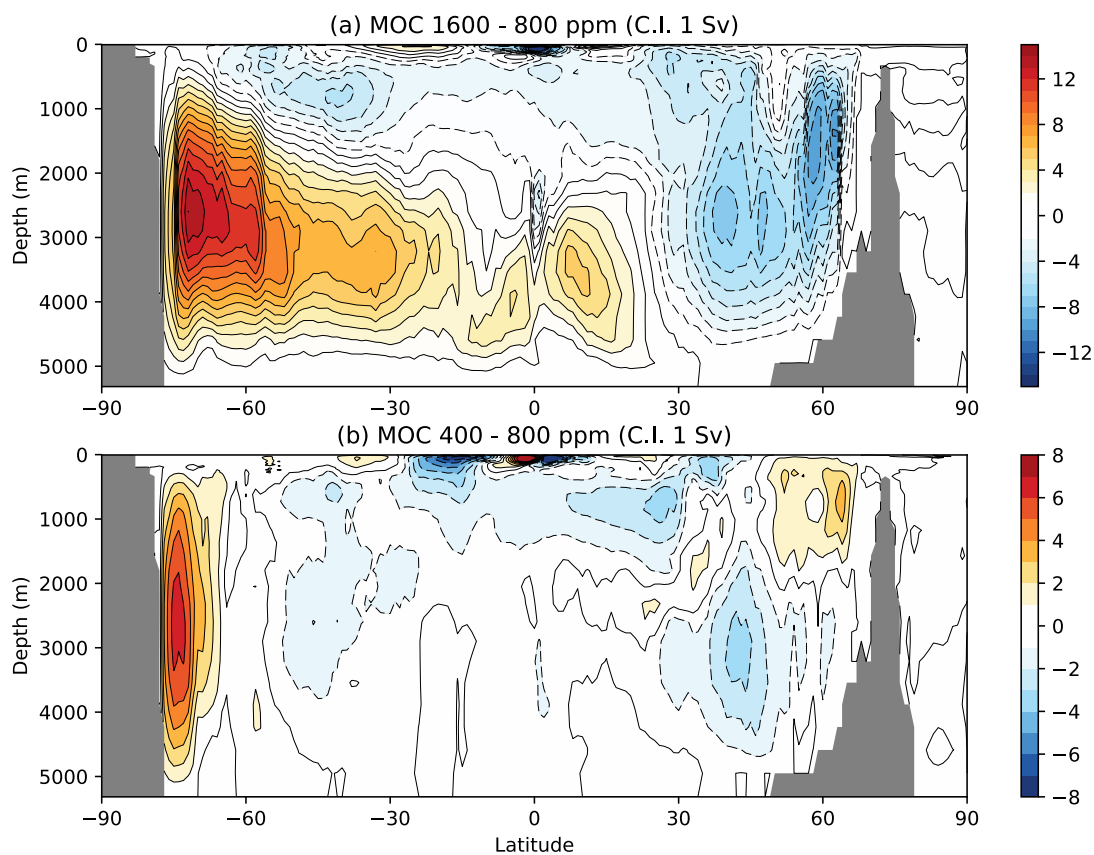
5

Climate
of the Past
Discussions

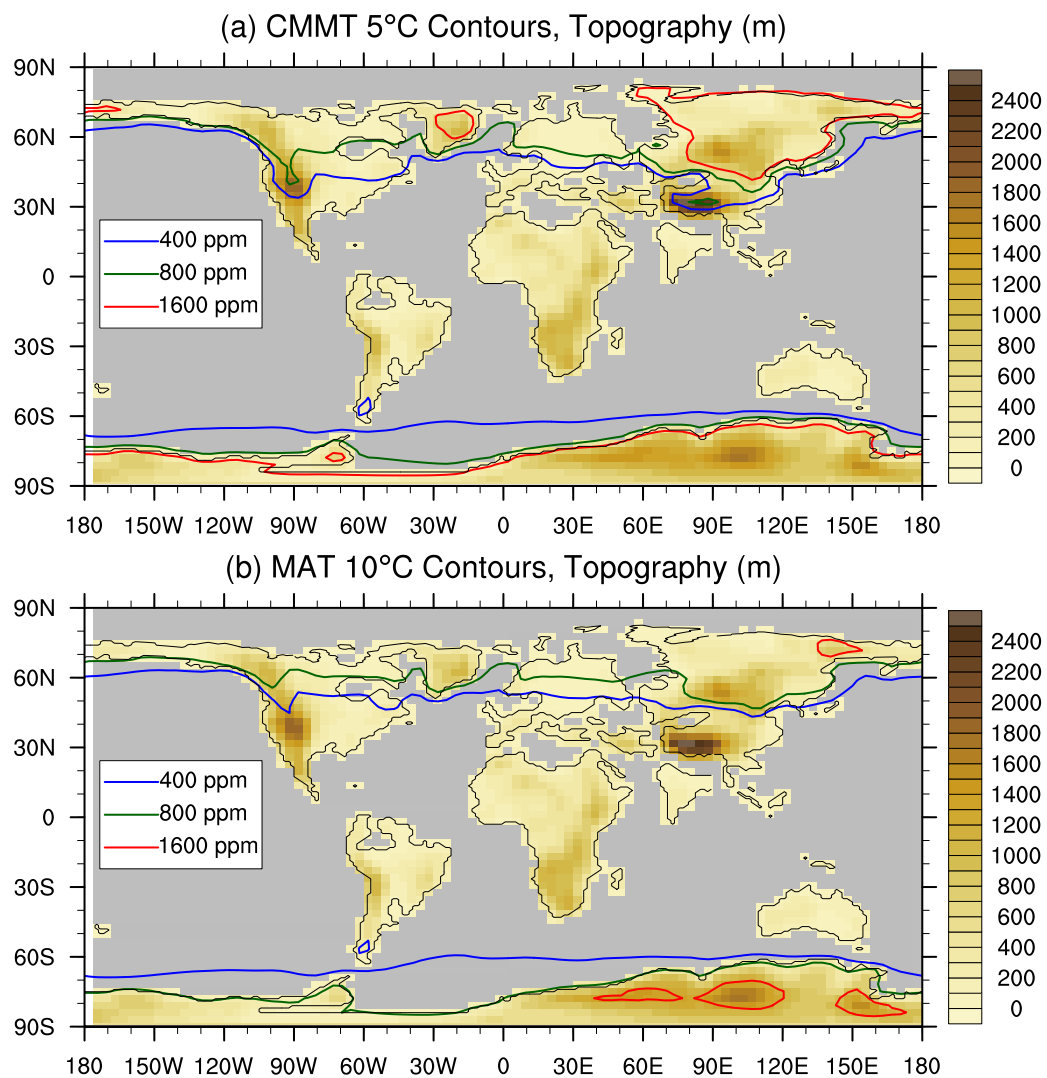Figure 12: Difference in global MOC in response to (a) doubling and (b) halving CO_2.

Figure 13: Minimum temperature thresholds for the palm/cycad line, showing (a) cold month mean temperature (CMMT) contours of 5°C and (b) mean annual temperature (MAT) of 10°C.